UNIVERSIDADE FEDERAL DO PARANÁ

LÉCIO VICENTE MONTANHEIRO

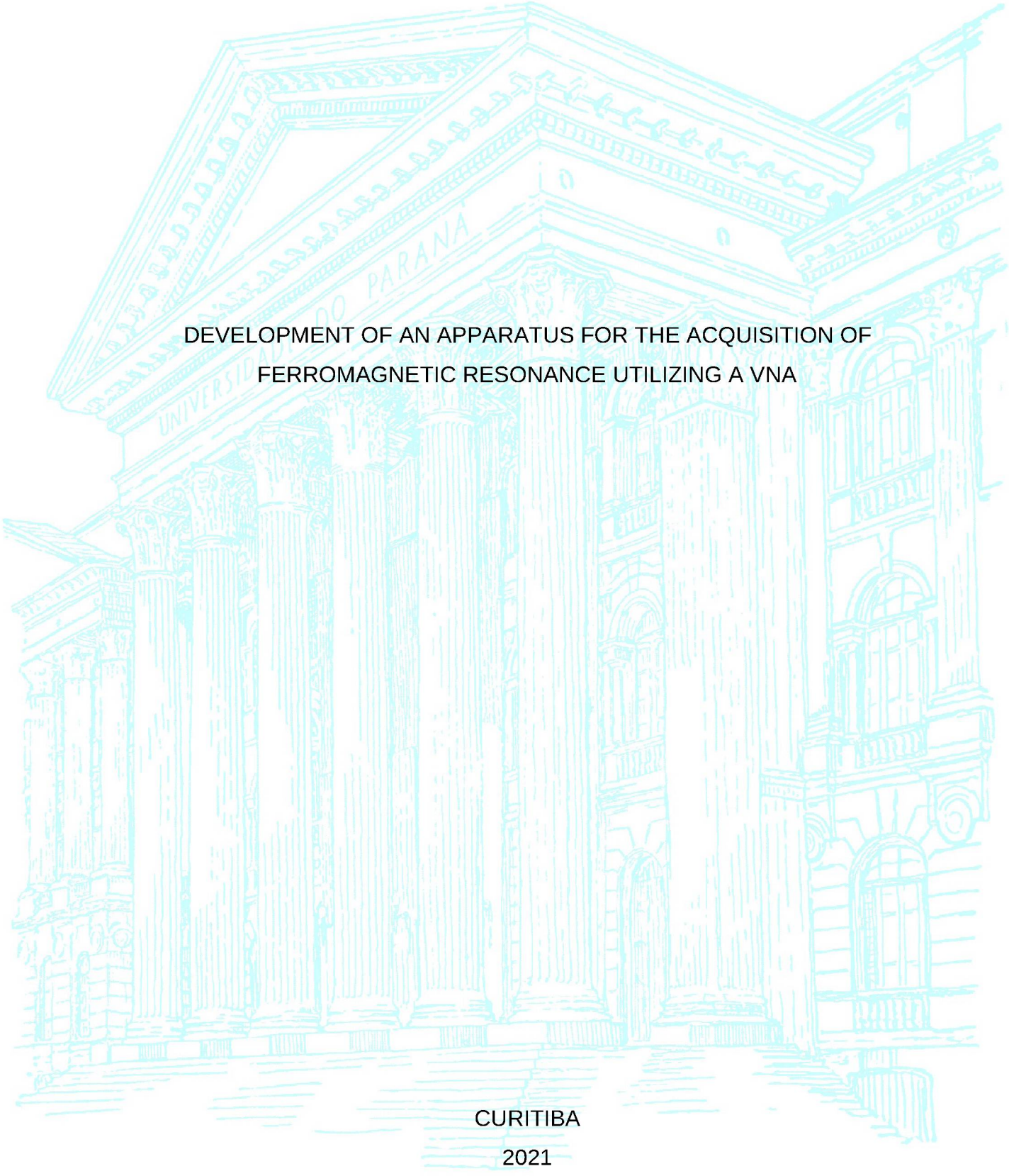

DEVELOPMENT OF AN APPARATUS FOR THE ACQUISITION OF FERROMAGNETIC RESONANCE UTILIZING A VNA

CURITIBA

2021

LÉCIO VICENTE MONTANHEIRO

DEVELOPMENT OF AN APPARATUS FOR THE ACQUISITION OF FERROMAGNETIC RESONANCE UTILIZING A VNA

Dissertação apresentada ao curso de Pós-Graduação em Engenharia Elétrica, Setor de Tecnologia, Universidade Federal do Paraná, como requisito parcial à obtenção do título de Mestre em Engenharia Elétrica.

Orientador: Prof. Dr. Marlio José do Couto Bonfim

Coorientador: Prof. Dr. César Augusto Dartora

CURITIBA

2021

Catalogação na Fonte: Sistema de Bibliotecas, UFPR
Biblioteca de Ciência e Tecnologia

M764d Montanheiro, Lécio Vicente
Development of an apparatus for the acquisition of ferromagnetic resonance utilizing a VNA [recurso eletrônico] / Lécio Vicente Montanheiro – Curitiba, 2021.

Dissertação - Universidade Federal do Paraná, Setor de Tecnologia, Programa de Pós-Graduação em Engenharia Elétrica.

Orientador: Marlio José do Couto Bonfim
Coorientador: Cesar Augusto Dartora

1. Ressonância ferromagnética. 2. Analise vetorial de redes. I. Universidade Federal do Paraná. II. Bonfim, Marlio José do Couto. III. Dartora, Cesar Augusto. IV. Título.

CDD: 537.62

Bibliotecária: Roseny Rivelini Morciani CRB-9/1585

MINISTÉRIO DA EDUCAÇÃO
SETOR DE TECNOLOGIA
UNIVERSIDADE FEDERAL DO PARANÁ
PRÓ-REITORIA DE PESQUISA E PÓS-GRADUAÇÃO
PROGRAMA DE PÓS-GRADUAÇÃO ENGENHARIA ELÉTRICA - 40001016043P4

TERMO DE APROVAÇÃO

Os membros da Banca Examinadora designada pelo Colegiado do Programa de Pós-Graduação ENGENHARIA ELÉTRICA da Universidade Federal do Paraná foram convocados para realizar a arguição da Dissertação de Mestrado de **LECIO VICENTE MONTANHEIRO** intitulada: **Development of an apparatus for the acquisition of ferromagnetic resonance utilizing a VNA**, sob orientação do Prof. Dr. MARLIO BONFIM, que após terem inquirido o aluno e realizada a avaliação do trabalho, são de parecer pela sua APROVAÇÃO no rito de defesa.

A outorga do título de mestre está sujeita à homologação pelo colegiado, ao atendimento de todas as indicações e correções solicitadas pela banca e ao pleno atendimento das demandas regimentais do Programa de Pós-Graduação.

CURITIBA, 08 de Dezembro de 2021.

Assinatura Eletrônica
17/12/2021 12:08:18.0
MARLIO BONFIM
Presidente da Banca Examinadora

Assinatura Eletrônica
16/12/2021 10:22:20.0
EDUARDO PARENTE RIBEIRO
Avaliador Interno (UNIVERSIDADE FEDERAL DO PARANÁ)

Assinatura Eletrônica
23/12/2021 13:47:03.0
VITORIA MARIA TUPINAMBA SOUZA BARTHEM
Avaliador Externo (UNIVERSIDADE FEDERAL DO RIO DE JANEIRO)

This work is dedicated to the great Mother Nature, giver and maintainer of our lives. The eternal teacher which fascinates us with its exact and uniform laws (though we do not know them exactly!) She who keeps us humble in our knowledge and forever active in our lives as researchers.

ACKNOWLEDGEMENTS

I thank my advisor Prof. Dr. Marlio José do Couto Bonfim for the laboratory hours and explanation hours spent with my elaboration of the apparatus, measurements, and electronics devices. His are also my thanks for the sample collection I was able to get my hands on. I also thank my co-advisor, Prof. Dr. Cesar Augusto Dartora, which helped me devise important parts of the mathematical foundation of ferromagnetic resonance (FMR). I also thank Physics Department professors Dante Mosca for GCPW Thales waveguide and cobalt $25\,nm$ sample and Ismael Graff for loaning us the coil system and controllable power supply which were crucial to attain FMR. To prof. Dr. Vitoria Maria T.S. Barthem my appreciation for the permalloy samples she prepared and relinquished to us in no time at all. To Stefania Pizzini from CNRS-Institut Néel-Grenoble for the cobalt 8Å samples she sent from France for our synchronized-field sweep apparatus benchmark. My formal thanks to the Department of Electrical Engineering of the Federal University of Parana for allowing me to work on my Master course as a way to improve my academic background in my position as a physics laboratory technician there. I also thank the Graduate Program in Electrical Engineering where I took this Master in Science program for the organization, support and professionalism as a whole...

RESUMO

Sinais de resonância ferromagnética foram observados pela primeira vez, mais de um século atrás, por V.K. Arkadiev em arames. Recentemente, a partir do interesse em utilizar o fenômeno na spintrônica, o estudo atingiu a escala de frequências em gigahertz em filmes nanométricos. Isto passou a exigir, naturalmente, equipamentos mais sofisticados. A ressonância ferromagnética é uma área de pesquisa bastante ativa mas a aquisição de seu sinal requer um aparato complexo e demorados ajustes. A técnica VNA-FMR foi empregada neste trabalho para a aquisição de sinais FMR de várias amostras, inclusive de espessura na escala de angstrons. Uma técnica de aquisição de sinais discreta e outra contínua foram desenvolvidas com a última atingindo melhores resultados que a primeira numa fração do tempo original e com melhor resolução. Guias de onda/ porta-amostras microstrip e GCPW foram utilizados, todos dimensionados para uma impedância $50\,\Omega$. Aquisições foram realizadas até $18\,GHz$, o final da escala do VNA utilizado. Amostras de permalloy e cobalto-platina foram analisadas e seus dados compilados. A caracterização FMR incluiu o coeficiente de atenuação de Gilbert, o fator-g, a magnetização de saturação e anisotropia magnética.

Palavras-chave: Ressonância ferromagnética, Analisador vetorial de redes, Novo aparato de medição, Parâmetros de espalhamento S, Coeficiente de atenuação de Gilbert, Amostra com espessura de angstrons.

ABSTRACT

Ferromagnetic resonance signals have been first observed more than a century ago by V. K. Arkadiev on wires, and recently, from the interest on utilizing the phenomena on spintronics, it has scaled up to gigahertz frequencies and nanometric sizes. This, of course, has been met by increasingly sophisticated measurement requirements. Ferromagnetic resonance is a very active research area but its acquisition requires a complex apparatus and lengthy tweaking. The vector network analyzer (VNA)-FMR technique was employed in this work to acquire FMR signals from several samples down to angstrom dimensions. A field-discrete and a field-synchronous technique were explored whereas the later achieved in a few seconds acquisition a whole FMR lorentzian at increased resolution. Microstrip and GCPW sample-holders were utilized, all designed to meet a 50 Ω impedance. Measurements were performed up to 18 GHz, the maximum frequency the available VNA was able to source. Permalloy and Cobalt-Platinum samples were analyzed and their FMR data compiled. FMR characterization included the Gilbert attenuation coefficient, g-factor, saturation magnetization and magnetic anisotropy.

Keywords: Ferromagnetic Resonance, Vector Network Analyser (VNA), Novel measurement apparatus, S Scattering Parameters, Gilbert Attenuation Coefficient, Angstrom thick sample.

LIST OF FIGURES

LIST OF TABLES

LIST OF ABBREVIATIONS AND ACRONYMS

CPW	CoPlanar Waveguide
FMR	Ferromagnetic Resonance
FWHM	Full Width Half Maximum
GCPW	Grounded CoPlanar Waveguide
GMR	Giant MagnetoResistance
IP	In Plane
LLG	Landau-Lifschitz-Gilbert (equation)
MOKE	Magneto Optical Kerr Effect
MTJ	Magnetic Tunnel Junction
NMR	Nuclear Magnetic Resonance
OC	Open Circuit
OOP	Out Of Plane
PIMM	Pulsed Inductive Microwave Magnetometry
PSU	Power Supply Unit
PWM	Pulse Width Modulation
QUCS	Quasi Universal Circuit Simulator
SC	Shorted Circuit
SCPI	Standard Commands for Programmable Instruments
SMA	SubMiniature type A (connector)
STT	Spin Transfer Torque
TE	Transverse Electric (wave)
TEM	Transverse ElectroMagnetic (wave)
TL	Transmission Line
TRMOKE	Time Resolved MOKE
VNA	Vector Network Analyzer

SUMMARY

1

Introduction

Charge carrying electronics will sooner or later meet its demise (WALDROP, 2016) as new areas of physics and electrical engineering run to meet Moore's law in computing density power (DIETL et al., 2009). Spintronics is one of such areas and works on the premise of dealing with the electron's spin property as an element of information carrying unit (CHAMBERS, 2002). Its obvious advantage is that any circuit running under spintronics phenomena will cause no Joule effect, therefore, no heating of elements will be observed and no heat dissipation strategies need to be employed at all. Miniaturization to angstrom dimensions (CHO; GOODSON, 2015) is then, a physical possibility.

The use of magnetic materials spreads over a myriad of technological applications (HECK, 2013), ranging from the fabrication of high-efficiency inductors, transformers and microwave circulators to magnetic memories and giant magnetoresistance (GMR) devices (XIANG et al., 2002; AKERMAN et al., 2003; MONTAIGNE et al., 1998; MIYAZAKI; TEZUKA, 1995; ZHANG et al., 1997; MOODERA; NOWAK; VEERDONK, 1998; G..., 2002; DARTORA; CABRERA, 2005; DARTORA; CABRERA, 2008). The state of the art in advanced magnetic materials includes nanostructured multilayered devices and magnetic thin films. Therefore, the characterization of the magnetic properties and hysteretic loops of these materials is of fundamental importance and several experimental techniques are currently available. For instance, low frequency characterization can be understood within the scope of electrical circuit theory, for which the dynamic magnetic susceptibility of a given magnetic material is straightforwardly obtained by performing inductance measurements. On the other hand, a much more sophisticated approach for magnetic characterization is the use of the so-called magneto-optic Kerr effect (MOKE) (HUBER; SCHÄFER, 1998), which consists of measuring the polarization rotation of light reflected at the surface of the material under test. Given the fact that the frequency of the electromagnetic waves used in MOKE lies in the optical domain, one effectively probes thick ($\sim 50\,nm$) layers of slowly time-varying magnetization of the samples.

Despite having being first observed more than a century ago (ARKADIEW, 1923),

ferromagnetic resonance (FMR) is an intense area of research interest, a Google scholar search for the expression "Ferromagnetic resonance" returned 1980 results only for the year 2021 (this was written in September/2021). Its principle has been widely used to ascertain ferromagnetic materials behavior (FANG et al., 2011). The theory behind FMR is considerably straightforward and can be obtained classically (POLDER, 1949) By vector multiplying the magnetic fields present in a radio frequency (RF) microwave signal and an externally applied one and then deriving energy difference levels caused by the Zeeman effect on the corresponding electron at which point one applies the Landau-Lifshitz-Gilbert equation. One can find a nuclear magnetic resonance (NMR) parallel explanation in Guimaraes (GUIMARãES, 2000).

1.1 Motivation

FMR signal processing allows for the pure science study of ferromagnetic materials and their properties like the g-factor, the gyromagnetic ratio or the Gilbert attenuation coefficient α. Through these one can also delve in investigations involving the contributions of spin and orbital motions to the material's magnetic moment.

Of immediate research interest, magnetic memories developments are a hot research area where FMR-mediated acquisition of physical quantities like α are helpful when designing such memories.

There are several magnetic memory building techniques. The newer ones rely on experimental physics phenomena like spin-valve, spin-transfer torque (STT) and magnetic tunnel junctions (MTJ). They all aim to trap spin orientation as an information bit. The goal is, of course, to increase information density within materials. Old methods relied on magnetic hysteresis, they were slow and and did not reach modern day required information storage densities. All newer magnetic memories techniques are tied to α's value which dictates maximum rates for reading, writing and minimum memory refresh rates as spin states need to remain unaltered between these events.

Two other FMR acquisition techniques are mentioned in this work: Pulsed Inductive Microwave Magnetometry (PIMM) and Resonant Cavity. Both require extensive post-processing and, for Resonant cavity, allow for very few data points over frequency, because it requires a different resonant cylinder for every different frequency. VNA-FMR uses only the VNA as a complex instrument as it simultaneously sources and measures signal at the ends of the waveguide. Its built-in lock-in-amplifier sports up to 24-bit I/O signal handling making available a resolution of 6 parts per billion. Far more than what is necessary for this work. VNA-FMR allows the experimenter to scan for DC field resonances at any frequency within the VNA's range. That provides as many data points

as the experimenter wishes to fit Kittel and Gilbert curves, thus decreasing measurement uncertainties.

Of particular interest, VNA-FMR, acquires data extensively over a broad frequency spectrum, allowing for narrower uncertainty values. In this work, two apparatuses have been developed to acquire these quantities, they were named step-field sweep and synchronized-field sweep. The goal of any apparatus development is to either increase easy-of-use or to achieve better resolutions. The field-synchronous technique achieved both. It is a fast to results technique, yielding double the resolution of the step-field sweep technique.

Similar phenomenon, Electron Paramagnetic Resonance (EPR) is usually able to utilize the same apparatus as FMR as both sense resonance in unpaired electrons. Both phenomena have very near gyromagnetic ratios. EPR relies on whole Zeeman energy shifts perceived by electrons. These shifts happen at external magnetic field dependent frequencies. EPR detection is dependent on high resolution instruments as only a very small quantity of atoms in the sample will have unpaired electrons in an exact energy level to flip at the given Zeeman energy sourced. In this regard FMR is a much more responsive phenomena as all magnetic moments in a small sample will be aligned to the external field. Nonetheless, EPR is applicable to a wider range of elements and materials as it works on paramagnetic materials whereas FMR only works on ferromagnetic ones. Nuclear Magnetic Resonance (NMR) is yet another resonance based investigative technique but this one is based on unpaired nucleons which also have a response to a Zeeman splitting energy. Despite a nucleon mass being 2000 times that of an electron, the arm distance of their orbits is next to negligible. As the gyromagnetic ratio may be defined as the ratio between a particle's dipole moment to its angular momentum, it is easy to see that the gyromagnetic ratio (γ) one works under NMR will be some orders of magnitude smaller than that under FMR. As a matter of fact, a free electron's γ is around $28 GHz/T$ whereas a proton's γ is 42 MHz/T.

As denoted by this very work on section 4.3, it is completely possible to retrieve FMR signals from angstrom-thick films. One of the samples tested was characterized by an 8Å cobalt layer, since metallic cobalt is an hcp organized crystal with $c = 0.406\,nm$, a thin film of 8Å has really only two layers of cobalt atoms.

1.2 Objectives

As stated before, FMR has drawn much attention as a magnetic characterization tool (FANG et al., 2011). Several techniques were developed in the last 100 years and VNA-FMR systems have reached the capability of analyzing nanometric thin films

(MAKSYMOV; KOSTYLEV, 2015). A technique used for a very long time was that of the resonant cavity (MAKSYMOV; KOSTYLEV, 2015). This technique has the major disadvantage of being able to only irradiate samples at quite a few frequencies, namely, the frequencies for which the enclosure develops resonant modes. This method was able to return few FMR $[H_{res}; frequency]$ data points and relied of the magnetic field sweep to look for resonances. VNAs paired with planar waveguides brought increased capabilities for FMR investigations as now it is possible to acquire hundreds of data points since planar waveguides pose little impediments to frequency variation (MAKSYMOV; KOSTYLEV, 2015). Curiously, under planar waveguides techniques the resonant modes are the ones to avoid. More points allow for better curve fittings and higher resolutions therefore.

1.2.1 General Goal

To develop a FMR acquisition apparatus based on a VNA (TAMARU et al., 2018) having an arduino controller board to drive a controllable power supply and to receive field data from gaussmeter.

1.2.2 Specific Goals

- A simpler FMR acquisition technique is planned to be used at first, it is meant to acquire ~ 50 curve points in a point-per-point scheme. Time consuming as it is it is meant to be this work's first attack at the problem;
- A second technique is to use an arduino micro-controller's built-in pulse width modulation (PWM) function to send a square wave to the PSU. The PSU will then amplify this signal accordingly the PSU's front panel settings and submit the coils to the resulting current;
- Microstrip and GCPW waveguides are to be built to act as I_{RF} magnetic field generators since FMR arises in a material exactly because a second field, non-collinear to the DC one, causes a precession in electron spin movement. The frequency of this precession being the Larmor frequency, denoted by f.
- Thin film, nanothick, ferromagnetic (FM) samples are to be sought for testing;
- A software interface is to be developed to avoid interfering with the experiment and help organize data and streamline results;
- A lorentzian curve is to be fitted to the returned $[S_{21}, DCField]$ values. Its peak value will denote the resonant H_{res} field for the frequency against which it was

tested. Testing for several different frequencies will allow the researcher to fit $[H_{res}; frequency]$ data to what is called a Kittel fitting . This fitting will return g-factor g (or gyromagnetic ratio γ) and effective magnetization M_{eff}.

- Full width half maximum (FWHM) values obtained from the acquired lorentzians are to be plotted against frequency and then return the Gilbert attenuation coefficient α, a much sought after, dimensionless, value. Comparing these data to the literature will validate the apparatus.

1.3 History

Popularly, whenever a layman person says a magnetic material, he means a ferromagnetic one. Magnets, magnetite specifically, have been reportedly found in China two and half millennia ago (SHU-HUA, 1954), making it one of the first science topics ever. Later on observed in Greece supposedly when shepherds noticed particular stones that were attracted by their shoe's iron nails. Give it some centuries and magnetite was then used as a compass' needle, telling travelers where the Earth's magnetic south pole was and by doing so, allowing them to know which direction they were going to. Nowadays magnetism has been scientifically fathomed up to the core of quantum physics, nonetheless its macroscopic behavior deriving from interactions between discrete magnetic domains it remains a phenomenological area, predictable in detail only by software simulations.

FMR has been first observed by Russian physicist (self called magnetologist) V. K. Arkadiev in experiments he developed on iron and nickel wires between 1911 and 1913 (published 1919)(ARKADIEW, 1923). He correctly attributed the selected absorption bands of microwaves to the resonance of elementary carriers of magnetic moment. This makes FMR a science topic already more than a century old. Many other physicists (many of them Soviet) worked on it and substantially improved the theory through experiment and theory. Ya. G. Dorfmann for instance suggested FMR a quantum explanation in 1923, attributing FMR's resonance energy as surfacing from the valence-electron (DORFMANN, 1923) now switching between two non-degenerate Zeeman discrete energy levels. In 1935, L. Landau and E. Lifshitz proposed a new phenomenological formulation for the dynamics of interaction between magnetic moments in a ferromagnetic material and have thus predicted FMR for nickel (LANDAU; LIFSHITZ, 1935). Later on the phenomena acquired its experimental validation in a 1946 J.H.E. Griffiths article (GRIFFITHS, 1946).

2

Fundamentals

2.1 Magnetism

All matter has a magnetic response, be it paramagnetic, diamagnetic, ferromagnetic, ferrimagnetic, anti-ferromagnetic or others. These behaviors arise from multiple sources: interaction between magnetic domains, Eddy currents, exchange energy. Rather than analytical solutions these behaviors are usually analyzed in novel materials through experimentation and variations are predicted then through finite element simulation (FISCHBACHER et al., 2007; CORTÉS-ORTUÑO et al., 2018).

Magnetic behavior arises, microscopically, classically (AHARONI et al., 2000), from magnetic moment vectors generated by electrons spin and orbit around an atom's nucleus and interactions imprinted on them such as the Pauli exclusion principle. When submitted to an external magnetic field these magnetic moments will tend to align, showing ferromagnetism; slightly align when it is the case of paramagnetism; or anti-parallel alignment of vectors such as in ferrimagnetism and anti-ferrimagnetism (KAHN, 1993).

Most of the magnetic response is caused indeed by the electron's spin, being the orbital contribution very small and in ferromagnetic materials it corresponds to only a few percent points (SÖDERLIND et al., 1992) of the total magnetic moment. FMR is characterized as the precession suffered by an electron at a Larmor frequency to which it is subjected because of an external magnetic field (YALÇIN, 2013). Rather than theoretically calculate this effect contribution to a material's magnetic behavior, this work focuses on the energy absorption characteristics this phenomena causes through FMR itself.

Magnetic materials are mathematically classified through the magnetic susceptibility χ physical quantity (See figure 1. χ positive values denote how much a material's magnetization vector is prone to align itself constructively to an external field strength vector. Positive responses,$\chi > 0$, will classify the material as paramagnetic whereas negative ones,$\chi < 0$, will indicate the material as diamagnetic. A strong positive magnetic

response,$\chi >> 0$, classifies the material as ferromagnetic. Many sources actually understand ferromagnetism to be a sub-type of paramagnetism. Indeed, ferromagnets will turn into paramagnets above the Curie point (or Curie temperature) T_C. It is a very common thought to question why are there not other ferromagnetic elements, for example, why is manganese not a ferromagnetic element? The answer is not very simple indeed. From the whole periodic table of elements, only the aforementioned three: iron, cobalt and nickel have net interatomic forces that make them naturally align themselves towards one only magnetization vector.

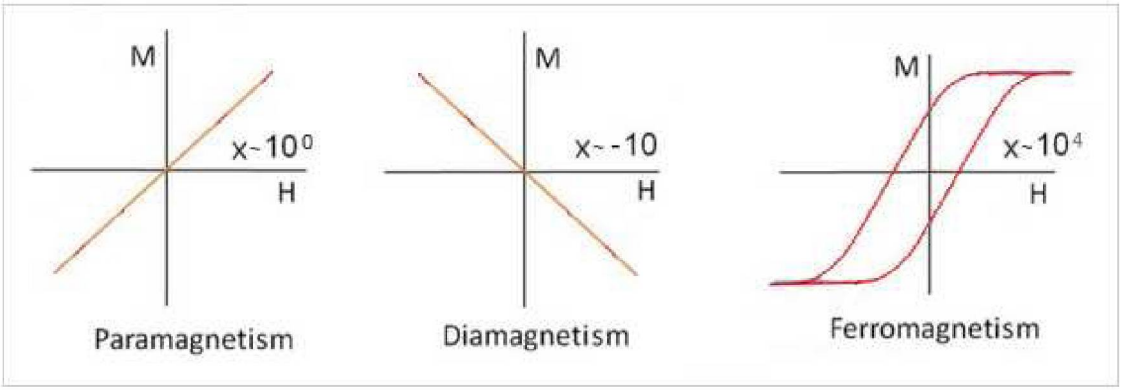

Figure 1 – Most common magnetic behaviors in relation to magnetic susceptibility χ

2.1.1 Diamagnetism

Diamagnetism is characterized by a material's repulsion to an external variable field (SPALDIN, 2010). It will be made noticed in the presence of an external field and works as modeled in Lenz' law. This law states that a z-positive axis variation of an external B field will trigger a xy-plane clockwise induced current which will in turn generate an opposing field. The induced electrical current will be found on the material's atom-core-bound electrons and also on the free, cloud electrons. It is worth noting that most metals are actually diamagnetic mainly due to their abundant free electrons cloud.

Diamagnetism is modeled with negative susceptibility factor and magnetic permeability only because of its counter field effect. It is easy to show that this signal comes straight from Lenz' law. This type of magnetism is not an easy one to isolate. In all truth, all materials have a proportion of their magnetic behavior diamagnet (SPAIN, 2014). But all other types of magnetism: ferromagnetism, paramagnetism, etc. bear stronger magnetic susceptibility than diamagnetism (BUSCHOW; BOER et al., 2003). Thus, resolving diamagnetic behavior from the other types of magnetism becomes a no trivial task. That is the reason diamagnetism has been studied mostly on materials that show very weak (or not present at all) signals of the other behaviors.

As most other forms of magnetism, diamagnetism is actually a quantum effect. Classically speaking all diamagnetic materials have an even number of electrons distributed electronically in a way that for every energy level there is an equal number of up and down spins. This would lead to the conclusion that there would be no net magnetic moment left in such materials. Under quantum mechanics though (E., 2014), an external field produces a subtle shift in energy levels of two orbit-sharing opposite-spins electrons such that a counter field is generated. Were it not for this, not all matter would exhibit some type of magnetic behavior.

2.1.2 Paramagnetism

Paramagnetism is characterized by a material's weak attraction to an external field. It might have several different sources and is overall an alignment of an atom's electronic magnetic moments, either spin or orbital sourced to a preferred, external, direction. Paramagnetic materials show a linear behavior with an external field. As its susceptibility is very small, external fields would need to be on the order of μ_0 to reach a saturation plateau. Looking at figure 2 (LEHMANN, 2008) one can figure paramagnetism as dependent on outer incomplete electron shells and verify that in paramagnetism one finds one or more non-paired electrons. Extending this comprehension, it is also possible to say that the further out the radius of such electrons (orbitals d, f) the higher the original field will be amplified. A classical description based on the fact that the magnetic moment is directly dependent on an electron mean orbital radius.

2.1.3 Ferromagnetism

Ferromagnetism is considered a form of paramagnetism. Indeed what causes it to show large magnetic susceptibilities is that in ferromagnetic materials one atom's (or molecule) net magnetic moment influences its neighbors' magnetic moments to start pointing in the same direction. This raises magnetic susceptibility numbers from tens to thousands. There are only three, room temperature, ferromagnetic elements: Iron, Cobalt and Nickel. However many of these elements alloys are also ferromagnetic. Other two elements which also exhibit ferromagnetism are Gadolinium and Dysprosium, the former shows a Curie point of 292 K, the latter a 88 K one. Manganese alloys very often also show ferromagnetic behavior.

Magnetism was for many decades thought out as a classical phenomena but is indeed a quantum one. It raises from magnetic moments generated from unpaired electrons in a given energy level. As can be derived from figure 2, iron electronic distribution is [Ar] $3d^6 4s^2$. That results in 4 unpaired, d orbital electrons. Cobalt, [Ar] $3d^7 4s^2$ results

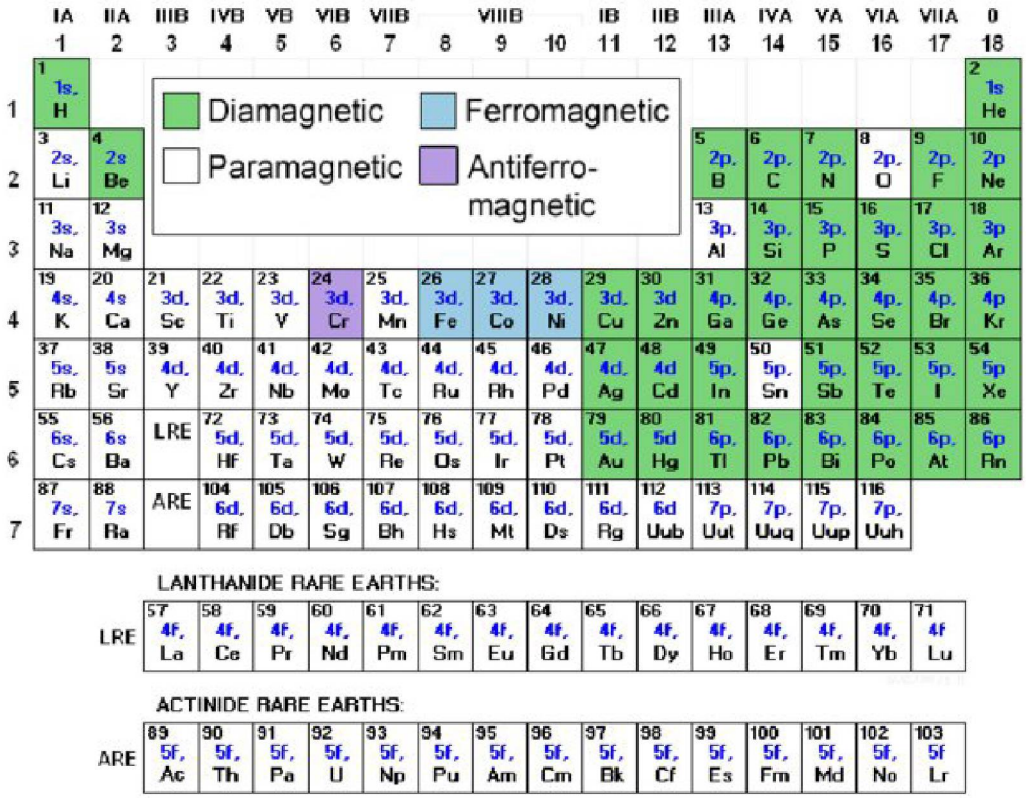

Figure 2 – Table of elements indicating magnetic behavior (LEHMANN, 2008)

in 3 and Nickel, [Ar] $3d^8 4s^2$ results in 2. As is the case in ferromagnets, neighboring atoms influence one another in order to reach a spontaneous dominant net magnetization throughout a sample. Higher inter-atomic lattice distances would allow for electron clouds to not overlap and therefore to not cause spins to pair accordingly Pauli's exclusion principle and in doing so, canceling each other's magnetic moments. These simple observations do not explain ferromagnetism in its entirety at all and are mentioned as a means to a classical physical intuition. The modern day description of ferromagnetism rests on the exchange energy J_{ex} concept, which arises when two electrons from two adjacent atoms come close enough to each other to establish a minimum energy constructive wavefunction interference bonding between them (KRISHNAN, 2016). This energy is plotted against the electron's distance on a graph known as the Bethe-Slater Curve, seen on figure 3.

On the Bethe-Slater (KRISHNAN, 2016) curve one sees the three room-temperature ferromagnetic elements α-iron bcc (body-centered cubic), cobalt and nickel as well as gadolinium ($T_C = 292\ K$) all possessing a positive J_{ex} factor, making them consonant to ferromagnetic behavior. On the other hand, γ-iron (also called austenitic iron) which displays an FCC (face-centered cubic) lattice structure sees a decrease in inter-atomic distance and its J_{ex} energy, accordingly to the overlapping premise, falls below zero.

Manganese and chromium also sport lattice constants smaller than that of γ-iron and the curve correctly deems them as also non-ferromagnets. Such sharp change in magnetic behavior over so little physical differences, named one unit in atomic number or bcc to fcc lattice constants, points to a good description of the phenomena.

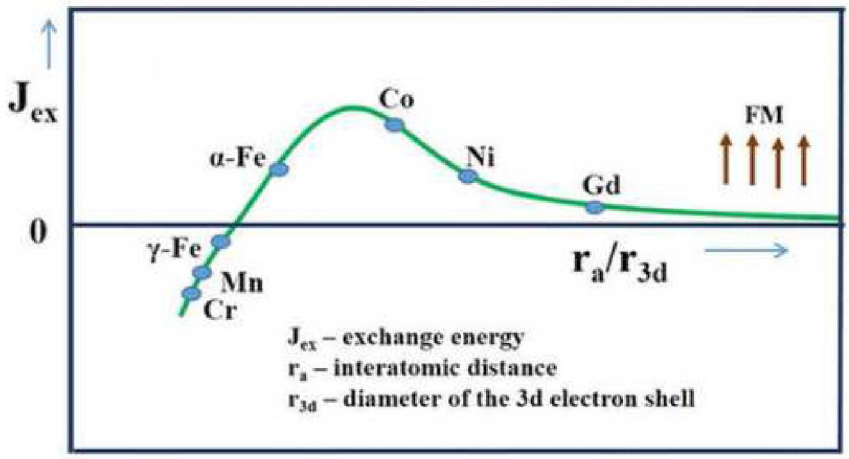

Figure 3 – The Bethe-Slater Curve. Adapted from (CHAUDHARY; RAMANUJAN, 2016)

Bethe has described ferromagnetism this way and developed a practical graph showing how exchange energy as a function of inter-atomic distances elicits iron, cobalt and nickel apart from the other elements (KRISHNAN, 2016). Despite magnetic classification holding an apparent relation to their position in the Periodic Table of Elements as seen in figure 2, this correlation fleets precise understanding of magnetic behavior. (CARDIAS et al., 2017) and others have revisited the Bethe-Slater curve and their calculations show that fermi-level electrons in lattice-organized $[Ar]3d^{4-8}$ atoms interactions need more scrutiny when calculating exchange energy.

The exchange energy or exchange integral is dependent on how much an electron wavefunction overlaps those of its neighbors. In crystal structured materials this overlap will also depend on the distance between neighboring atoms, i.e., the crystal atomic spacing. Further research in the area now takes into account the mean orbital radius of an atom's several orbitals contributing for or competing against ferromagnetic behavior.

2.2 Zeeman Effect

Ferromagnetic resonance relies fundamentally on the splitting of same-energy electrons into doublets or triplets when subjected to an external DC field. This typifies the Zeeman effect, a subtle shift in energy levels of electrons in such a way that relaxation

of these electrons raise cause to slightly shifted emission lines (SPALDIN, 2010). There are historically two variations of the Zeeman effect. The so-called Normal Zeeman Effect, where one sees spectral emission lines shifted $m_l = 1$ apart, from all possible $m_s = 2l + 1$ and the Anomalous Zeeman Effect, named before spins had been theorized. In anomalous mode, visible under stronger magnetic fields, the energy variations include spin discrete energies. Both modes are actually effects of the same cause, the energy absorbed from the magnetic field increases the system's magnetic moment strength. This increase, if significant enough, will then force the affected electrons to occupy neighboring available quantum energy slots. Ferromagnets, the material studied by this work, show the so-called anomalous Zeeman effect as at their last energy level one finds many non-spin-paired electrons. Mathematically the contributions of the anomalous effect to the net magnetic moment comes both from the orbital angular momentum and the spins angular momentum whereas in the normal effect the spins cancel each other out. As ferromagnets magnetism arises fundamentally from its net spin moments, their modeling will be that of anomalous considered with zero orbital moment.

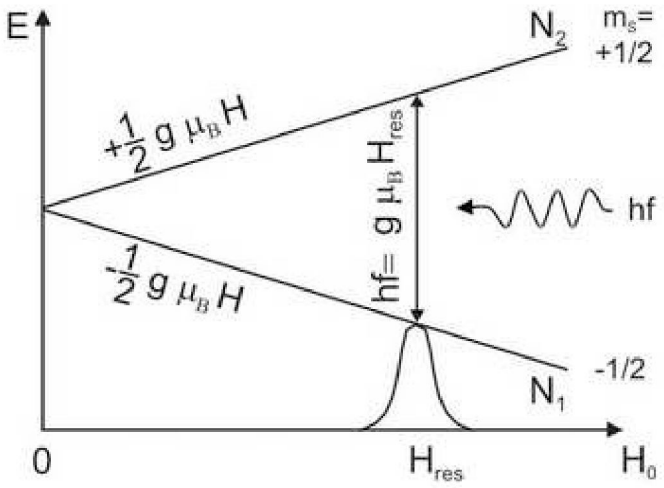

Figure 4 – Spin based Zeeman effect diagram. Adapted from (SPERLICH, 2013).

Under a regular Zeeman Effect there is an energy shift for a single bound electron on an s orbital equal to:

$$\Delta E = -\mu.\mathbf{B} \tag{2.1}$$

which is just the atom's original net magnetic moment μ now under a dot product with an external applied oriented magnetic field $\mathbf{B}$. Taking the total magnetic moment of the system to be that of equation 2.12, one reaches:

$$\Delta E = g_S \, \mu_B \, SB \tag{2.2}$$

Where g_S is the g-factor, μ_B is the Bohr magneton, S is the Poynting vector and B is the external magnetic field.

2.2.1 Magnetic Moment

The magnetic moment generated by an orbiting charged particle may be derived from its mean angular momentum as both these quantities share the same unit direction vector perpendicular to the orbiting plane. One can also understand the magnetic dipole moment (or plain magnetic moment as no monopole has ever been detected) as just a convenient way to encase the characteristics of a current loop. The magnetic moment μ is then, defined as:

$$\mu = IA \tag{2.3}$$

where I is the current that travels the loop and A is the area encased by it. Substituting the electron charge $-e$, area $A = \pi r^2$, particle velocity v in 2.3 one obtains:

$$\mu = \frac{-ev}{2\pi r}\pi r^2 = \frac{-evr}{2} \tag{2.4}$$

Adapting for the angular momentum L, where m_e is particle's (in this case, an electron) mass

$$L = m_e v r \tag{2.5}$$

one reaches

$$\mu = \frac{-e}{2m_e}L \tag{2.6}$$

Since quantum physics also obliges the quantization of the angular momentum L in the z direction as $L_z = m\hbar$, the magnetic moment μ will suffer this restriction too and become:

$$\mu = \frac{-e}{2m_e}m\hbar \tag{2.7}$$

Which establishes the Bohr magneton when $m = 1$

$$\mu_B = \frac{-e\hbar}{2m_e} \tag{2.8}$$

2.2.2 g-factor

The Bohr magneton is a constant defined on the fundamental state of the hydrogen atom out of convenience for the notation of magnetic moments for the other elements. As such, it was introduced the g-factor, a dimensionless proportionality factor that characterizes the ratio of an atom's (or molecule) magnetic moment to that of hydrogen's.

Moreover, the same way that the magnetic moment is described as a discrete proportion of the quantum number m, it is then possible the describe it as a proportion of the spin number s or orbital number l or a combination of the two. In metals and metal-alloys such as the Iron-Nickel (permalloy) the majority of the contribution to μ comes from the spin of the unpaired electrons. As a comparison, in paramagnetic materials there are no spin-unpaired electrons and all the contribution to μ comes from the orbitals, hence their weak magnetic susceptibilities. Defining **S** and **L** as:

$$S = \hbar\sqrt{s(s+1)} \tag{2.9}$$

$$L = \hbar\sqrt{l(l+1)} \tag{2.10}$$

And substituting 2.10 and 2.8 in 2.6 one finds the orbital contribution to the magnetic moment:

$$\mu_L = g_L \frac{\mu_B}{\hbar} L \tag{2.11}$$

Similarly for the spin contribution:

$$\mu_S = g_S \frac{\mu_B}{\hbar} S \tag{2.12}$$

where g_L and g_S are the g-factor for the orbital and spin respectively.

The external magnetic field adds discretely to the magnetic potential energy of the electrons. As is the case in metals and low applied fields, the orbital contribution is next to negligible as ferromagnets get their behavior mostly from spin. So, the magnetic moment might be described as in equation 2.12.

2.2.3 Gyromagnetic ratio

Often confused with the g-factor, the gyromagnetic ratio is, as its name implies, the ratio of magnetic moment to angular momentum (ultimately spin and/or orbital). Usually denoted by the greek letter γ, this factor is very practical when experimentally guessing what $[B, H_{res}]$ pairs are reasonable to try. It is rigorously expressed in SI units $rad/s.T$ but experimentally more commonly seen in FMR as GHz/T. The equation below shows γ for a free electron, therefore, based solely on its spin angular momentum. Experimental γ values are determined taking the derivative of a Kittel fitting.

$$\gamma = \frac{g\,\mu_B}{h} \sim 28GHz/T \tag{2.13}$$

2.3 Ferromagnetic Resonance

Ferromagnetic resonance (FMR) is an energy absorption phenomena that relies on the Zeeman effect energy shift to happen (YALÇIN, 2013). Traditionally performed

using samples in resonant cavities (MAKSYMOV; KOSTYLEV, 2015), that when excited to the right frequency and magnetic field will absorb a small part of the energy of the exciting electromagnetic wave. This happens when its electrons start switching between quantized magnetic moments aligned within the external field B.

This switching happens between the magnetic moment fully aligned with B and one of its inferior quantum possible z-axis levels. If, then, the frequency of the applied electromagnetic wave matches that of new magnetic moment precession, the resonance establishes itself and will absorb an energy maximum until it relaxes to the ground state.

2.3.1 Lorentzian Modeling

FMR can be mathematically modeled as a lorentzian curve. Its physical quantities descriptors find in the lorentzian curve coefficients good matches and make it possible to directly recover resonance field values H_{res} (if frequency is kept constant or vice-versa) and the curve's linewidth, i.e., its waist at FWHM (Full Width at Half Maximum) which is a parameter for calculating how strong is the sample's attenuation of the ferromagnetic resonance. It stands to note that these coefficients are strongly related to the sample's geometry and as so they stray considerably from material's in-bulk properties. The Lorentzian curve (or Cauchy curve) is a peak finder function described by:

$$I(2\theta) = \frac{\omega^2}{\omega^2 + (2\theta - 2\theta_0)^2} \tag{2.14}$$

where $2\omega = FWHM$ and resonance happens at 2θ.

The actual FMR signal to a lorentzian fitting is more complicated as other physical sources of signal can hardly be unconsidered. Real acquired signals tend to suffer from drifting, which can be subtracted from the original signal and to show different start and finish lorentzian plateaus. The following equation is meant to deal with a differential form of an FMR signal:

$$\frac{dP}{dH_{DC}} = K1\frac{4\Delta H(H - H_{res})}{[4(H - H_{res})^2 + \Delta H^2]^2} - K2\frac{\Delta H^2 - 4(H - H_{res})^2}{[4(H - H_{res})^2 + \Delta H^2]^2} + drift + offset \tag{2.15}$$

Where P is the power lorentzian, H or H_{DC} is the swept field, H_{res} is the resonance field, K1 and K2 mute variables. Such differential signal can be seen on figure 26. Visually this representation leaves much to be desired. Its minimum and maximum do not represent linewidth limits and it is harder to identify the resonance peak as now it shows a maximum derivative value. Mathematically however, equation 2.15 automatically retrieves H_{res} and linewidth ΔH (WOLTERSDORF, 2004). It also retrieves these data already drift and offset free.

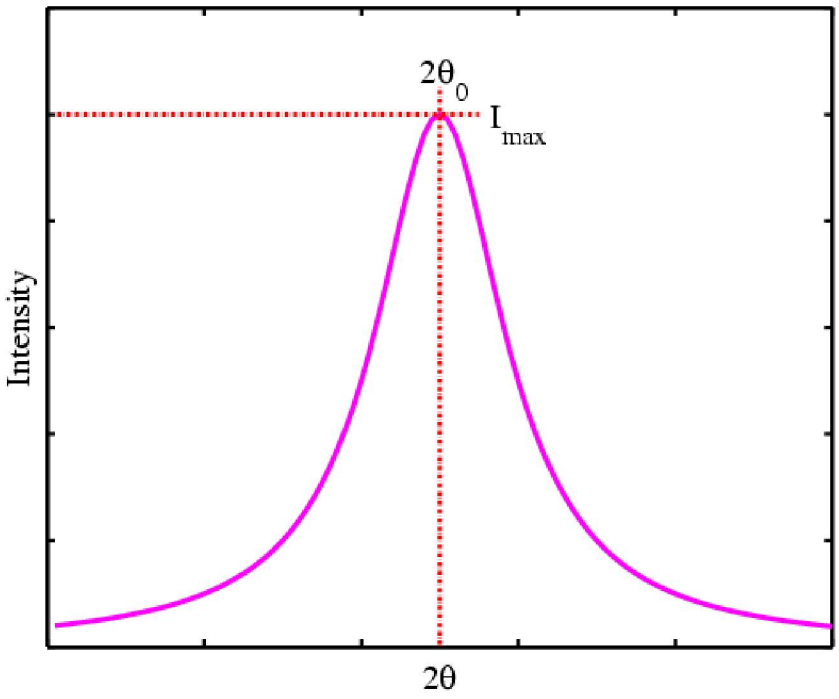

Figure 5 – Lorentzian curve graph (LEHMANN, 2008)

2.3.2 Kittel Fitting

Geometry of the sample plays along overall magnetization of the samples through the demagnetizing factors. These empirical factors stand on the fact that every magnetic field forms a closed loop and, therefore, the wider the sample is in the direction of the applied magnetic field, the more magnetic field lines (N_i) will return to the south magnetic pole through the material itself, effectively decreasing the internal perceived field (KITTEL, 1976). Magnetic fields in the direction i become then:

$$B_i^n = B_i^0 - N_i M_i \quad \text{with} \quad i = x, y, z \tag{2.16}$$

Applying this definition to equation 2.24,with $\eta = 0$ one reaches:

$$\frac{dM_x}{dt} = \gamma(M_y B_z - M_z B_y) = \gamma[B_{0z} + (N_y - N_z)M]M_y \tag{2.17}$$

$$\frac{dM_y}{dt} = \gamma[M(-N_x M_x) - M_x(B_{0z} - N_z M)] = -\gamma[B_0 + (N_x - N_z)M]M_x \tag{2.18}$$

Equal phase, exponentially decaying time dependent $e^{-i\omega t}$ solutions of the equations 2.17 and 2.18 exist if:

$$\begin{bmatrix} i\omega & \gamma[B_0 + (N_y - N_z)M] \\ -\gamma[B_0 + (N_x - N_z)M] & i\omega \end{bmatrix} = 0 \ , \tag{2.19}$$

Which returns:

$$\omega_0^2 = \gamma^2[B_0 + (N_y - N_z)\mu_0 M][B_0 + (N_x - N_z)\mu_0 M] \tag{2.20}$$

Now, taking $N_x = N_z = 0$ and $N_y = 1$, where the field is parallel to the surface, which characterizes IP (in plane) orientation, the following equation is reached:

$$f = \gamma\mu_0 \sqrt{H_{\parallel}(H_{\parallel} + M_{eff})} \tag{2.21}$$

And, taking $N_x = N_y = 0$ and $N_z = 1$, the case for field perpendicular to to surface (OOP orientation), one reaches:

$$f = \gamma\mu_0 \, H_{\perp}(H_{\perp} + M_{eff}) \tag{2.22}$$

where M_{eff} is the effective magnetization and γ, the gyromagnetic ratio.

Plotting this graph allows the retrieval of γ and M_{eff} from the experimental dataset through a numerical fitting. Kittel fittings are somewhat faulty because M_{eff} and γ are actually coupled and as such, the Kittel fitting admits several solutions which are close enough to the data points.

Typically plotted as:

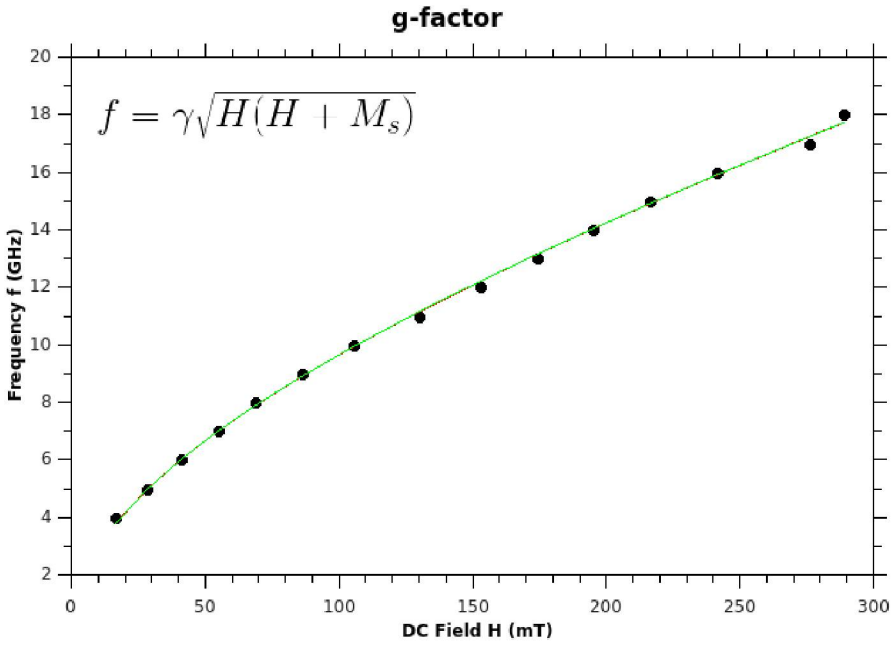

Figure 6 – Kittel fitting (LEHMANN, 2008). $\gamma = df/dT = 43.2\,GHz/T$ calculated between 16 and 18 GHz. Permalloy 100 nm. IP orientation.

2.3.3 Linewidth Fitting

The most sought after coefficient in recent years in FMR is the Gilbert attenuation coefficient α. A measurement of how fast an electron excited with the Zeeman effect returns to its previous state (GILBERT, 2004). This parameter is an experimental one and was added to the Landau-Lifshitz equation years later to better describe strong attenuation factors achieved with thin films for example. With a stronger attenuation comes the advantage of possible higher rates of bit switching (BARATI et al., 2013) for magnetic memories. This behavior coupled with the fact that α naturally increases the thinner a film is (NIBARGER et al., 2003), makes this geometry a good candidate for high data density, fast magnetic memories. Gilbert α attenuation coefficient is fitted through the following equation (YIN et al., 2015):

$$\Delta H = \frac{\alpha}{\gamma} f + \Delta H_0 \tag{2.23}$$

Typically plotted as:

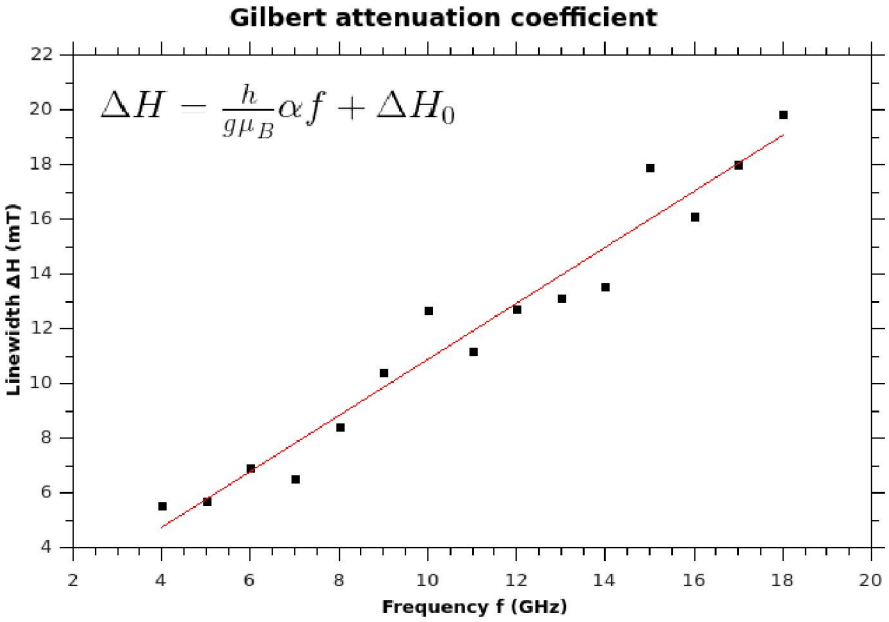

Figure 7 – Gilbert attenuation coefficient α

It is easy to see that the graph on figure 7 is a linear equation but the value of α will still depend on what will be retrieved for γ in the Kittel fitting. H_0 is an indicator of field dispersion within the sample.

2.3.4 Dynamic Magnetic Susceptibility

The magnetization dynamics of ferromagnets is qualitatively well described by the Landau-Lifschitz-Gilbert (LLG) equation (GILBERT, 1955; LANDAU; LIFSHITZ, 1935; LAKSHMANAN; NAKAMURA, 1984; ZHANG; LEVY; FERT, 202; GRINSTEIN; KOCH, 203; GLADKOV; BOGDANOVA, 2014):

$$\frac{\partial \mathbf{M}}{\partial t} = -\gamma[\mathbf{M} \times \mathbf{B}] + \gamma\eta\mathbf{M} \times \frac{\partial \mathbf{M}}{\partial t} \ , \tag{2.24}$$

where $\mathbf{M}$ is the magnetization vector, measured in A/m, γ is the gyromagnetic ratio, η is a parameter related to the damping factor and $\mathbf{B}$ is the magnetic flux density vector, measured in tesla. The term $-\gamma[\mathbf{M} \times \mathbf{B}]$ describes the precession

From classical electromagnetism, $\mathbf{B}$ is related to the magnetic field intensity $\mathbf{H}$ and the magnetization by the following relation:

$$\mathbf{B} = \mu_0(\mathbf{H} + \mathbf{M}) \ . \tag{2.25}$$

Equation (2.24) can be recast into the Landau-Lifshitz form, which is more suitable for the purposes of the present work, by replacing $\partial\mathbf{M}/\partial t$ in the last term of equation (2.24) by itself, as follows:

$$\begin{aligned} \frac{\partial \mathbf{M}}{\partial t} &= -\gamma\mathbf{M} \times \mathbf{B} + \gamma\eta \times \frac{\partial \mathbf{M}}{\partial t} \\ = -\gamma\mathbf{M} \times \mathbf{B} + \gamma\eta\mathbf{M} \times &\left[-\gamma\mathbf{M} \times \mathbf{B} + \gamma\eta\mathbf{M} \times \frac{\partial \mathbf{M}}{\partial t}\right] \\ &= -\gamma\mathbf{M} \times \mathbf{B} - \gamma^2\eta\mathbf{M} \times (\mathbf{M} \times \mathbf{B}) + \\ &\gamma^2\eta^2\mathbf{M} \times \left[\mathbf{M} \times \frac{\partial \mathbf{M}}{\partial t}\right] \ . \end{aligned} \tag{2.26}$$

Now, using the following vector product identity:

$$\mathbf{a} \times (\mathbf{b} \times \mathbf{c}) = (\mathbf{a} \cdot \mathbf{c})\mathbf{b} - (\mathbf{a} \cdot \mathbf{b})\mathbf{c} \ , \tag{2.27}$$

the last term of equation (2.26) can be rewritten as follows:

$$\mathbf{M} \times \left[\mathbf{M} \times \frac{\partial \mathbf{M}}{\partial t}\right] = -M^2 \frac{\partial \mathbf{M}}{\partial t} \ , \tag{2.28}$$

since $\mathbf{M} \cdot \frac{\partial \mathbf{M}}{\partial t} = 0$, which can be concluded by applying the dot product between $\mathbf{M}$ and equation (2.24). Notice the last equation warrants that $\mathbf{M} \cdot \mathbf{M} = M^2 = M_s^2$ is a constant, where M_s is known as the saturation magnetization. Now substituting (2.28) into (2.26) and rearranging the terms one gets:

$$\frac{\partial \mathbf{M}}{\partial t} = -\gamma_0\mathbf{M} \times \mathbf{B} - \alpha\mathbf{M} \times (\mathbf{M} \times \mathbf{B}) \ , \tag{2.29}$$

where $\gamma_0 = \gamma/(1+\gamma^2\eta^2 M_s^2)$ and $\alpha = \gamma^2\eta/(1+\gamma^2\eta^2 M_s^2)$.

Following, let us define the magnetic susceptibility for a linear and homogeneous material in frequency domain ω, through the relation between the i-th component of the magnetization, which is the material response (effect), and the components of the externally applied magnetic field $\mathbf{H}$, acting as the stimulus (cause). Mathematically stated, is given by:

$$M_i(\mathbf{r},\omega) = \sum_j \chi_{ij}(\omega) H_j(\mathbf{r},\omega) \ , \tag{2.30}$$

where $\chi_{ij}(\omega)$ are the components of the magnetic susceptibility tensor $\boldsymbol{\chi}(\omega)$, which is a 3×3 matrix. It can be related to the magnetic permeability tensor by the relation $\boldsymbol{\mu}(\omega) = \mathbf{1} + \boldsymbol{\chi}(\omega)$, where $\mathbf{1}$ is the 3×3 identity matrix.

Now, the externally applied magnetic fields being given, the posed problem is to obtain the components χ_{ij} of the susceptibility tensor (the response function of the medium), by solving (2.29), which is non-linear and leads to chaotic behavior in a highly non-linear regime, often solvable only by numerical methods. Therefore, to obtain the frequency domain magnetic susceptibility in closed analytical form, the LL equation must be linearized. Fortunately, the physical scenario is amenable to such an approximation. Usually, the magnetization dynamics can be linearized in the presence of a magnetic field containing a high magnetostatic (or DC magnetic) field component, which nearly saturates the sample along the magnetostatic axis, denoted by z. This way, the mathematical problem resumes to solving for the transverse components of the magnetization (M_x, M_y), driven by a sinusoidal time-varying transverse magnetic field. Mathematically stated, the total applied magnetic field $\mathbf{H}$ can be decomposed into a magnetostatic component H_0 along the z-axis, superimposed to an RF magnetic field $\mathbf{h}(t) = (h_x, h_y, 0)$, whose components are in the (x,y)-plane, under the condition $H_0 >> |\mathbf{h}(t)|$. This way, the magnetization is nearly oriented along the z-axis, being determined by the DC magnetic susceptibility, $M_z = \chi_z^0 H_0 = M_0$, but the transverse components $\mathbf{M}_\perp = (M_x, M_y)$ can rotate due to the RF field and the magnetization vector precesses. Decomposing the magnetization and magnetic fields as follows:

$$\mathbf{B} = \mu_0 \mathbf{h}(t) + B_0 \hat{\mathbf{z}} \ , \tag{2.31}$$

$$\mathbf{M} = \mathbf{M}_\perp + M_0 \hat{\mathbf{z}} \ , \tag{2.32}$$

where $B_0 = \mu_0(H_0 - f_g M_0)$ is the internal magnetostatic flux density, f_g is a demagnetizing factor depending on the sample geometry, and $M_0 >> |\mathbf{M}_\perp|$. In what follows it is interesting to remember a few results of the transverso-longitudinal decomposition

algebra:

$$\mathbf{M}_\perp \cdot \hat{\mathbf{z}} = \mathbf{h}_\perp \cdot \hat{\mathbf{z}} = 0, \tag{2.33}$$

$$\mathbf{M}_\perp \times \hat{\mathbf{z}} = (M_y, -M_x) \ , \tag{2.34}$$

$$\mathbf{h} \times \hat{\mathbf{z}} = (h_y, -h_x) \ , \tag{2.35}$$

$$\mathbf{M}_\perp \times \mathbf{h}_\perp = (M_x h_y - M_y h_x)\hat{\mathbf{z}}. \tag{2.36}$$

Furthermore, if one is interested in the linear regime terms of the form M_x^2, M_y^2 or $M_x M_y$ can be neglected, taking into account that $M_0 >> M_x, M_y$. Also, since $M_z \approx M_0$ and $M_x^2 + M_y^2 + M_z^2 = M_0^2$, temporal variations of M_z will be discarded, i.e., $dM_z/dt \approx 0$ within the linear regime approximation. It is left as an exercise for the reader to show that, inserting (2.31) and (2.32) into (2.29) and taking the above mentioned facts into consideration, the LL equation will be reduced to the following linear equation, for the transverse components of the magnetization:

$$\frac{d\mathbf{M}_\perp}{dt} = -\mu_0\gamma_0 M_0 \hat{\mathbf{z}} \times \mathbf{h} - \gamma_0 B_0 \mathbf{M}_\perp \times \hat{\mathbf{z}} - \alpha(M_0 B_0 \mathbf{M}_\perp - \mu_0 M_0^2 \mathbf{h}) \ , \tag{2.37}$$

where terms proportional to $\mathbf{M}_\perp \cdot \mathbf{h}$ and $\mathbf{M}_\perp \times \mathbf{h}$ were neglected and $\mathbf{M} \times (\mathbf{M} \times \mathbf{B}) \approx M_0 B_0 \mathbf{M}_\perp - \mu_0 M_0^2 \mathbf{h}$. For harmonic time-varying fields $\mathbf{h} = \mathbf{h}_0 e^{i\omega t}$ and $d/dt \to i\omega$, such that:

$$\mathbf{M}_\perp = \frac{-\chi_z^0 \omega_0 \hat{\mathbf{z}} \times \mathbf{h} - \omega_0 \mathbf{M}_\perp \times \hat{\mathbf{z}} - \alpha\mu_0 M_0^2 \mathbf{h}}{i\omega + \nu} \ , \tag{2.38}$$

where $\omega_0 = \gamma_0 B_0$ is the cyclotron frequency, $\mu_0\gamma_0 M_0 = \chi_z^0 \omega_0$ and $\nu = 1/\tau = \alpha M_0 B_0$ is the inverse of the relaxation time τ. To solve the above equation it is enough to substitute the transverse magnetization $\mathbf{M}_\perp$ appearing in the second term of the right-hand side numerator by (2.38), which allows one to obtain:

$$\mathbf{M}_\perp = \frac{-\chi_z^0 \omega_0 \hat{\mathbf{z}} \times \mathbf{h} - \alpha\mu_0 M_0^2 \mathbf{h}}{i\omega + \nu} + \frac{\omega_0}{(i\omega + \nu)^2}(\chi_z^0 \omega_0 \hat{\mathbf{z}} \times \mathbf{h} + \omega_0 \mathbf{M}_\perp \times \hat{\mathbf{z}} + \alpha\mu_0 M_0^2 \mathbf{h}) \times \hat{\mathbf{z}}. \tag{2.39}$$

Using $(\mathbf{M}_\perp \times \hat{\mathbf{z}}) \times \hat{\mathbf{z}} = -\mathbf{M}_\perp$, and decomposing the equation into components yields:

$$M_x = \chi_{xx} h_x + \chi_{xy} h_y, \tag{2.40}$$

$$M_y = \chi_{yx} h_x + \chi_{yy} h_y, \tag{2.41}$$

where:

$$\chi_{xx} = \chi_{yy} = \frac{\chi_z^0 \omega_0^2 - \alpha\mu_0 M_0^2 (i\omega + \nu)}{\omega_0^2 + \nu^2 - \omega^2 + 2i\omega\nu} \ , \tag{2.42}$$

$$\chi_{xy} = -\chi_{yx} = \frac{\chi_z^0 \omega_0 (i\omega + \nu) - \alpha\omega_0\mu_0 M_0^2}{\omega_0^2 + \nu^2 - \omega^2 + 2i\omega\nu} \ . \tag{2.43}$$

This way, the dynamic permeability tensor can be put into the following form:

$$\boldsymbol{\mu}(\omega) = \begin{pmatrix} \mu_\perp & \eta & 0 \\ -\eta & \mu_\perp & 0 \\ 0 & 0 & 1 \end{pmatrix} , \tag{2.44}$$

where the values $\mu_\perp = 1 + \chi_{xx}$ and $\eta = \chi_{xy}$. Therefore, by measuring the permeability tensor, one is able to determine ω_0 and M_0, since ω is the known RF frequency and $\gamma = q/(2m)$ only depends on the charge (q) to mass (m) ratio of the particles carrying magnetic moment in the material. The resonant frequency is given by $\omega_r = \sqrt{\omega_0^2 + \nu^2} = \gamma B_0 \sqrt{1 + (\alpha^2/\gamma^2) M_0^2}$. For $\nu << \omega_0$ the expressions for $\mu_\perp$ and η can be simplified to:

$$\mu_\perp \approx 1 + \frac{\chi_z^0 \omega_0^2}{\omega_0^2 - \omega^2 + 2i\omega\nu} , \tag{2.45}$$

$$\eta \approx \frac{i\chi_z^0 \omega_0 \omega}{\omega_0^2 - \omega^2 + 2i\omega\nu} . \tag{2.46}$$

One can show, using Maxwell's equations, that the eigenstates of polarization in this anisotropic scenario will not show linear polarization, but elliptic in character. An initially linearly polarized wave will rotate its polarization vector, due to the Faraday effect. However, for small samples compared, Faraday rotation will be neglected and, for a linearly polarized electromagnetic wave with $h_y = 0$, the imaginary part of $\mu_\perp$, denoted by $\mu_\perp''$, will be related to the losses in the microwave propagation (from Poynting's vector), due to material absorption, being the dissipated power density given by:

$$P_{dis} = \frac{1}{2}\mu_0 \mu_\perp'' \omega |h_x|^2 = \mu_0 \frac{\chi_z^0 \omega^2 \omega_0^2}{(\omega_0^2 - \omega^2)^2 + 4\omega^2\nu^2} |h_x|^2 . \tag{2.47}$$

Notice that maximum absorption occurs at resonance $\omega = \omega_0$. Therefore, one can conclude that at resonance, microwaves will be the most absorbed and attenuated within the material.

2.4 S-parameters

In the present Section the theory behind the use of a VNA technique will be presented in more details. First of all, for the sake of completeness, a brief review of the scattering matrix **S** will be given. The description of S-parameters in the analysis of lumped-element networks was introduced in 1945 by the Russian-born mathematician and electrical engineer Vitold Belevitch in his PhD thesis (BELEVITCH, 1945; JOOS, 2000). At the same time the physicist and engineer Robert H. Dicke (MONTGOMERY; DICKE; PURCELL, 1947), which is famous for his contributions to general relativity and cosmology, developed the S-matrix theory while working on radar and coined the

term scattering matrix. The technique was made popular to the microwave engineering community by Kaneyuki Kurokawa (KUROKAWA, 1965) in the 1960s.

The idea behind the scattering matrix shows many similarities with the scattering matrix of quantum field theories, used to calculate the differential cross section of quantum particles collisions (GREINER; REINHARDT, 1996).

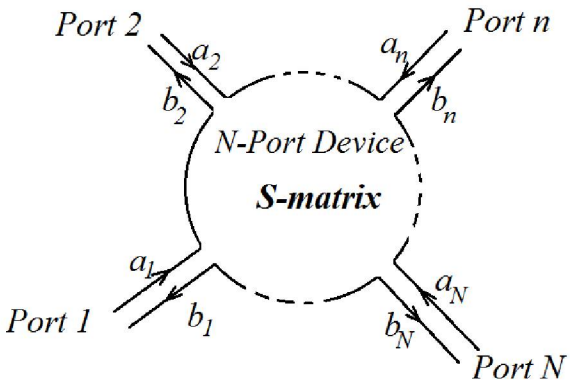

Figure 8 – A sketch of N-port device described by its S-matrix. The complex amplitudes a_n and b_n represent incoming and outgoing waves at port n. Source: the author.

The mathematical description of the S-parameters will follow closely the notation employed by D. M. Pozar (POZAR, 2012). Consider an N-port system, sketched in Figure 1, for which the the voltage V_n and current I_n at the n-th port is the superposition of forward (incident or incoming) and backward (reflected or outgoing) propagating waves. Mathematically it can be stated as follows:

$$V_n = V_n^+ + V_n^- , \tag{2.48}$$

$$I_n = I_n^+ + I_n^- = \frac{1}{Z_n}(V_n^+ - V_n^-) , \tag{2.49}$$

where V_n^+ and V_n^- are the voltage complex amplitudes of the incoming and outgoing waves at the n-th port, respectively, Z_n is the n-th port matching impedance. Usually, the voltage and current waves are normalized so that they can be measured in the same units. To to that, the voltages are divided by $\sqrt{Z_n}$ and the currents multiplied by $\sqrt{Z_n}$, and the new variables a_n and b_n are introduced:

$$a_n = \frac{V_n^+}{\sqrt{Z_n}} , \tag{2.50}$$

$$b_n = \frac{V_n^-}{\sqrt{Z_n}} , \tag{2.51}$$

which represent normalized incoming and outgoing wave amplitudes at port n, respectively. Now, the amplitude b_n of outgoing wave at port n can be related to the amplitudes a_m

of the waves incident at the other ports, by the following equation:

$$\begin{pmatrix} b_1 \\ b_2 \\ \vdots \\ b_N \end{pmatrix} = \begin{pmatrix} S_{11} & S_{12} & ... & S_{1N} \\ S_{21} & S_{22} & ... & S_{2N} \\ \vdots & \vdots & \ddots & \vdots \\ S_{N1} & S_{N2} & ... & S_{NN} \end{pmatrix} \begin{pmatrix} a_1 \\ a_2 \\ \vdots \\ a_N \end{pmatrix}, \tag{2.52}$$

where S_{mn} are known as the scattering parameters, relating the outgoing wave amplitude at the m-th port to the incident wave amplitude at the n-th port. They can be measured by exciting the n-th port with an amplitude a_n and setting all the other wave amplitudes entering ports $k \neq n$ equal to zero, i.e., $a_k = 0|_{k \neq n}$. In a practical setup, this is accomplished by matching the impedance at all the $k \neq n$ ports. This procedure defines the parameter S_{mn} as follows:

$$S_{mn} = \left. \frac{b_m}{a_n} \right|_{a_{k \neq n}=0}. \tag{2.53}$$

The special case occurs for $Z_n = Z_0$ at all ports, i.e., all ports having the same matching impedance, making the distinction between a_n and V_n^+ superfluous. Typically, Z_0 is set to 50Ω. The diagonal parameters S_{mm} represent the relative complex amplitude of the reflected waves at port m while the off-diagonals $S_{mn}, m \neq n$ represent the amplitude of the electromagnetic wave transmitted from port n to port m. The S-matrix of an ideally lossless systems have the property of unitarity, i.e., $\mathbf{S}^\dagger = \mathbf{S}^{-1}$, such that $\mathbf{S}^\dagger\mathbf{S} = \mathbf{S}\mathbf{S}^\dagger = \mathbf{1}$, where $\mathbf{1}$ is the $N \times N$ identity matrix and $\dagger$ denotes hermitian conjugation.

Going further, more attention will be paid to the case of a 2-port system, for which the S-matrix is written explicitly as follows:

$$\mathbf{S} = \begin{pmatrix} S_{11} & S_{12} \\ S_{21} & S_{22} \end{pmatrix}, \tag{2.54}$$

where S_{11} and S_{22} are the reflection coefficients at ports 1 and 2, respectively, S_{21} and S_{12} are the transmission amplitudes from port 1 to port 2 and in the opposite direction, respectively. Notice that the first indice of the S-parameter represents the input port of the signal and the second the output port. The most basic 2-port system is a transmission line of length l, characteristic impedance Z_0, phase constant $\beta = \omega/v$ and attenuation constant α at the angular frequency ω, v is the electromagnetic wave velocity in the line. From symmetry principles (propagation axis inversion or reciprocity), it is required that $S_{11} = S_{22}$ and $S_{12} = S_{21}$. Also, using the definition for S_{mn} the transmission line will be matched at its ends, ensuring that $S_{11} = S_{22} = 0$. This way, the S-matrix reads:

$$\mathbf{S} = \begin{pmatrix} 0 & e^{-i\beta l - \alpha l} \\ e^{-i\beta l - \alpha l} & 0 \end{pmatrix}. \tag{2.55}$$

The phase factor βl can be explained quite easily due to the fact that a wave transmitted from the port 1 to port 2 must propagate a distance l at the speed v. It produces a

time delay $\Delta t = l/v$, which results in a phase factor $\omega\Delta t = \omega l/v = \beta l$. For a lossy line, propagation is also accompanied by exponential attenuation, which clearly depends on the transmission line length l. The parameters β and α depend on the materials being used to construct the transmission line and on geometrical aspects of the construction. For fixed geometry, variation of materials will induce changes in the attenuation constant of the line.

2.5 Common FMR acquisition methods

All measurement methods evolve to reach higher resolutions or to be able to detect novel physical quantities. That is not different about FMR measurement apparatuses. The first employed method, the resonant cavity, was used by Arkadiev in what is understood to be the first FMR signal acquisition. As his paper from 1919 explains he used thermocouple elements to detect the energy absorption by the wires inside an elliptical cylinder subjected to microwaves and a primary field supplied by the very wires coiled on one another. The pulsed inductive microwave magnetometer (PIMM) technique was developed in the 60's and submitted planar waveguides to pulses tens of nanoseconds long, these pulses attenuations would then be sensed by induction elements and conveniently triggered to an oscilloscope capable of sampling at tens of gigahertz. Time-resolved magneto optical Kerr effect (TRMOKE) shows even higher resolutions with the sample being magnetized by the incidence of laser pulses periods of a few hundreds of femtoseconds. Of course, these increases in resolutions comes at the cost of sophisticated equipment. VNA-FMR is latest technique addition to the FMR measurement apparatuses list. It features virtually endless $[H_{res}; frequency]$ data points acquisition, is able to investigate non-reflective materials, is source and sensor signal compatible by construction and simplifies the overall experiment assembly. Below, a short description of these methods.

2.5.1 PIMM

Pulsed Inductive Microwave Magnetometry was first developed in the 60's by Smith and Wolf (KOS; SILVA; KABOS, 2002; KALARICKAL et al., 2006). It works based on a fast pulse generator that will excite the sample through a planar waveguide. As is the case with VNA-FMR, PIMM is able to to characterize FMR at multiple microwave wavelengths (MAKSYMOV; KOSTYLEV, 2015). Its major drawback is that it requires time consuming post data processing as it retrieves time-domain data points in attenuated harmonics format. The Gilbert attenuation coefficient is retrievable analyzing that attenuation, seen on figure 9c. This harmonic oscillation are captured by the sensing coils, figure 9a, and measured by a high samples/second able oscilloscope. Both

equipment in this setup are very expensive. Figure 9a shows a schematic apparatus setup. Figure 9b and c show data acquired by (NEUDECKER et al., 2006). A 45 ps rise time pulse would be equivalent to a 22 GHz frequency. The pulse generator does not need at all this capability since the α resolution will benefit from additional harmonics peaks. Figure 9c shows that for this specific setup a 1.5 ns sensing time was observed, which converts to a 0.67 GHz sourcing rate.

For FMR purposes only the sourced pulse width is in relation to the frequency f. Indeed, $f = 7.5\,GHz$ corresponds to a pulse width of 133 ps. At these rates the oscilloscope would be able to sample only 30 readings in 1.5 ns so it is reasonable to conclude the experimenter makes other passes delaying the trigger between the the pulse generator and the oscilloscope 0.01 ps and another pass from 0.02 ps so to acquire the three-digits equally spaced data points shown.

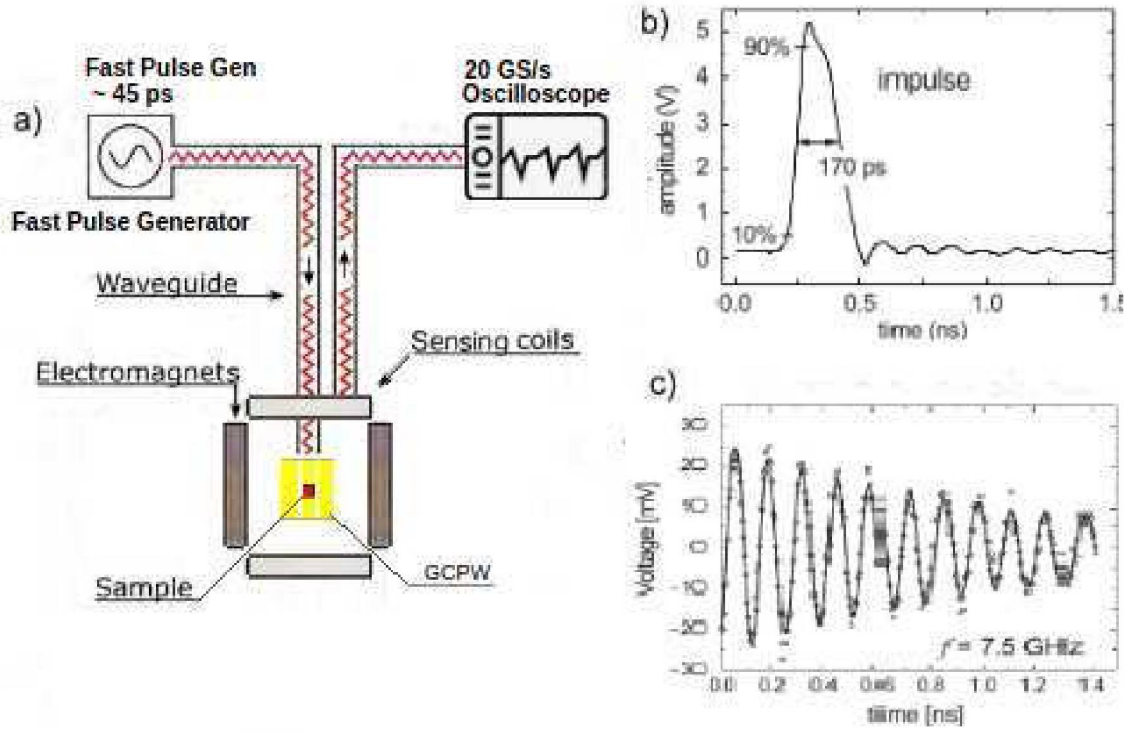

Figure 9 – a)Schematics of PIMM based FMR, b)Sourced Pulse, c) Attenuated harmonic wave. Data acquired by (NEUDECKER et al., 2006).

2.5.2 Resonant Cavity

Following figure 10, item a) shows a microwave source that is driven through a planar waveguide up to the sample itself. The waveguide acts both as microwave delivery

system and as a sample-holder as the sample is placed over it in a flipchip position. The sample is inside a closed conductive cavity.

The cavity supports some eigen-frequencies resonances to which the microwave source needs to be tuned to or a standing wave will not establish itself within the container (JENSEN, 2012). A transverse electrical (TE) mode standing wave is required so the sample becomes exposed to a maximum magnetic field halfway the cylinder height, in the symmetry axis (in TE_{11} mode). The TE mode shown on figure 10, letter b) is a TE_{11} mode. Both indexes: n,m in TE_{nm} refer to the number of half waves present in each cylindrical dimension. n applies to the azimuthal dimension and m to the radial one. It is easy to see then why this configuration shapes a single toroid. The cavity walls are placed were Bessel equations solutions show the electric field to be zero, thus making the walls non-absorbing waves (JENSEN, 2012). The drawing depicts the sample's main surface to be parallel to the external field. This positioning is named in-plane (IP).

The microwave circulator acts shifting entering microwave signals to the next port, that is, microwave source signals get shifted to the microwave cavity and microwave signals returning from the cavity get shifted to the diode detector which prevents possible reflected signals from being shifted to the source and acting constructively or destructively on it.

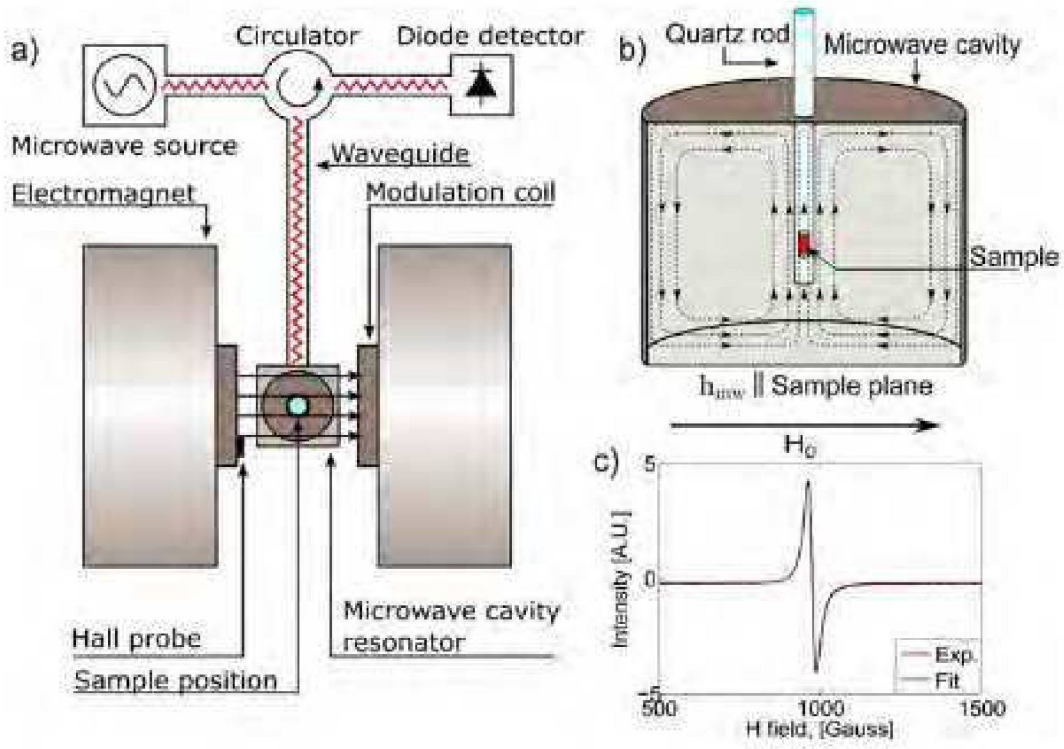

Figure 10 – a)Schematics of cavity based FMR, b)Cavity detail schematics, c) Permalloy differential FMR signal acquired with the technique (FLOVIK, 2016)

A quartz rod is used because they show strong reflective characteristics and thus do not cause a false increase, which would be frequency dependent, on absorption values.

The external DC field is supplied by a pair of coils right outside the cavity. Strong DC fields are notoriously difficult to reach and it is mandatory then that the coils gap be the smallest possible if one is to use portable equipment. In the figure the DC field sensor, the Hall probe, is placed outside the cavity. This is not the best layout as it can introduce minute variations in field reading but it is nonetheless minimized if the probe is still within a Helmholtz coil configuration volume. Modulation coils are actually a second set of coils that cause the actual variation of the net DC field experienced by the sample. Typically the non-varying coils will supply a saturation field, which is mandatory to achieve FMR and the modulation coils will provide a variable component field.

This setup requires field swept scans. On figure 10c) there is a differential plot of FMR signal as a function of such field sweep.

2.5.3 VNA-FMR

VNA-FMR acquisition works (KALARICKAL et al., 2006) by way of guiding an electromagnetic wave of known power and frequency through a planar waveguide over which a ferromagnetic thin-film sample lays. This EM is both sourced and sensed by a VNA. An external, independent, magnetic field is applied to the sample to generate a Zeeman effect in it and allow then for the search of a specific frequency with which the net magnetic moment carrier electrons will resonate in a precession movement. An absorption at a point $[frequency f, H field]$ identifies a ferromagnetic resonance and a subtle power dip will be sensed of the VNA B port, showing a smaller than 1 transmission parameter S_{21} as is drawn in figure 11a. In this schematic portrayal of a VNA-FMR acquisition setup one can identify the inverted lorentzian curve in the VNA, a coplanar waveguide (CPW) planar waveguide also in fig. 11a, where the sample in red rests within the signal track. A cross-section of the sample on the waveguide (COONROD; RAUTIO, 2012) highlights the h_{rf} field generated by the microwave displacement current through the sample. Fig. 11c shows a Kittel fitting graph of a Lanthanum strontium manganite oxide (LSMO) (FLOVIK et al., 2016), also known as perovskite. The inset shows a typical resonance point at $f = 4.8 GHz$; $H_{res} = 70 mT$. The schematics of fig. 11a show the layout between sample and H field to be parallel. That is confirmed by the typical Kittel fitting pointing to a zero intercepto-y.

Another mode of data acquisition is frequency sweep. The experimenter sets an H value and varies the frequency searching for the typical lorentzian curve in the acquired data. As the VNA calibration showed to be more sensitive to a new frequency than to a new H field, this work opted for a field swept operation.

VNA-FMR allows for probing at a multitude of frequencies, which provides for a better resolution in numerically fitted quantities as the g-factor or saturation magnetization M_s and the Gilbert coefficient α. Planar waveguides in their simplest shapes only require a double copper sided, high electrical permittivity (ϵ_r) substrate PCB. The waveguide may be etched on it by a chemical process or by mechanical milling. Simple GCPWs layouts show little attenuation up to $20\,GHz$.

Resonance signals in VNA-FMR are captured either sweeping the frequency at a constant field or the other way around, sweeping the field at a constant frequency. This work has adopted the latter in both instances of signal acquisition herein developed.

This work has developed a variation over the field-sweep that is able to show data in real time. It works through a synchronous cycle variation of the H field with a fixed frequency. This method allowed for immediate visualization of the lorentzian resonating curve on the very VNA screen in real time.

A sample's FMR investigations can be performed with the H field either orthogonal to the sample's surface or parallel to it. The results are different for each case because thin films characterize at best a two-dimension object and therefore, sport soft (IP) and hard (OOP) magnetic axes. Planar waveguides allow for the investigation of both and also, intermediate angles.

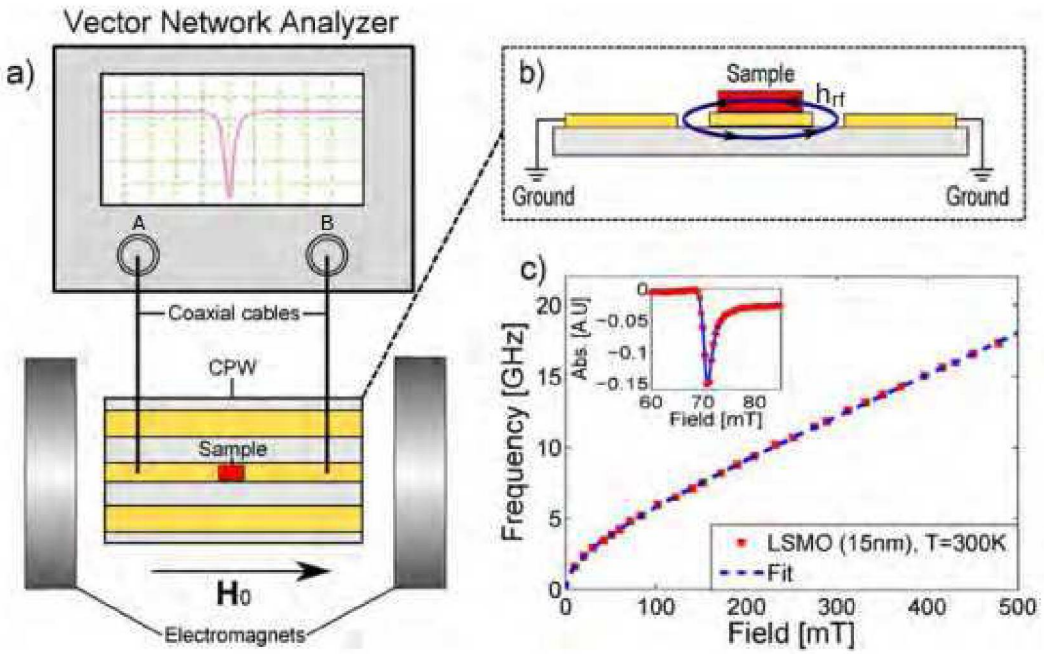

Figure 11 – a) Apparatus schematics of a VNA-FMR implementation. b) The FM sample is indicated in red over the CPW cross-section. c) Kittel fitting of a $La_{0.7}Sr_{0.3}MnO_3(LSMO)$. The inset shows a single, field swept, S_{21} curve at $4.8GHz$ (FLOVIK, 2016)

Resonance curves were reconstructed from the transmission coefficient S_{21}. Taking EM emission to be negligible one can state that:

$$Transmission + absorption = 1, \tag{2.56}$$

and so, since S_{21} is transmission, absorption becomes:

$$Absorption = 1 - S_{21} \tag{2.57}$$

Absorption represents then the energy sunk in the Zeeman effect. S_{21} parameter is already a normalized number and so the result is already a proportion.

2.6 Planar Waveguides

Planar waveguides as striplines, microstrip and coplanar waveguides (CPW) are a much more convenient sample holder and EMW carrier than resonant cavity sample holders. Differently from resonant cavities, planar waveguides are able to work over a large EM spectra and behave considerably within the restrictions of 2D carriers. They are therefore a very good apparatus-wise match for the VNA-FMR. However, as FMR returns tiny signals, very often of parts per thousand, line-impedance matching becomes important. Industry standard of 50Ω was adopted as well and the microstrips and CPWs have been calculated to match this impedance for a mean 9 GHz frequency. Several factors impact impedance magnitude and complex impedance. The most important of them are the dielectric losses and resistance caused by the skin depth effect (COONROD; RAUTIO, 2012).

2.6.1 Stripline

Striplines did not made it to be evaluated by this work as they are not easy to fabricate. Their main advantage is to enclose the sample completely between two dielectric layers and because of it, there is no delay of magnetic field lines that are, for instance, traveling through air in part of their closed loop around microstrips.

2.6.2 Microstrip

Microstrips is basically an EM conductor track over a high electrical permittivity substrate (MALORATSKY; LINES, 2000). Despite the EM having some of its magnetic field traversing the air, it showed less than 2% in propagation delay. This delay could have

an impact in S_{21} measurements since it could cause a mismatch between $S21$ and time readings. Nonetheless this delay would have no impact on the Gilbert coefficient since resonance points do not change based on EM power. A drawing of microstrip architecture can be seen on figure 12a.

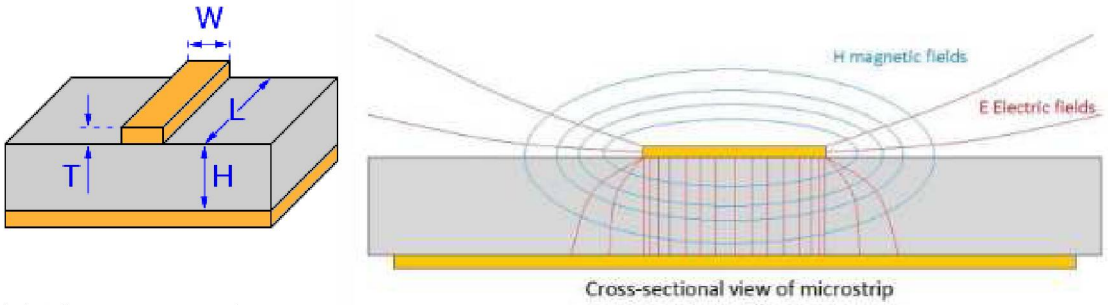

(a) Microstrip architecture as seen on Quasi universal circuit simulator (QUCS).

(b) Cross-section of generated fields on a Microstrip. Blue lines represent magnetic field lines. Red lines represent electric field lines. Yellow boxes represent copper or other conductor.

Figure 12 – Microstrip waveguide cross-section layout

The VNA-FMR experiment relies on the magnetic field generated by the I_{RF} (radio frequency current) traversing the thin film sample above it and thus, magnetizing it. The desired effect is for a significant amount of volume of the sample to be homogeneously magnetized so that a reasonable amount of molecule's magnetic moments enter resonance and actually drain enough power from I_{RF} to reach the apparatus measurement resolution. An schematic of the fields generated by microstrips can be seen on figure 12b.

Microstrips are easy to fabricate, they can be milled or chemically etched from PCBs, and connectors can easily be soldered on its edges. PCBs are available in various configurations of copper depth, substrate depth and with a choice of high permittivity materials. Most of the measurements in this work have been acquired with microstrips milled out of common, consumer electronics store grade, PCBs. Their dimensions were calculated with QUCS (BRINSON; JAHN, 2009) to reach a 50Ω impedance for a median frequency value of 9 GHz.

Microstrips are quasi-TEM (transverse EM) waveguides (ZHANG et al., 2016), devices that show some "leakage" of EM fields in the direction of propagation, but in the calculus performed on section 2.3.4 it was admitted no longitudinal generation of magnetic nor electric fields. In this situation it would be interesting to run simulations to try and predict possible strongly non-homogeneous points on the microstrip. Their numbers would be somewhat proportional to frequency. As a matter of fact for a sub-nano cobalt layer sample, the apparatus was unable to recover recognizable FMR signals

beyond 11 GHz where γ proportion said the system should be able to retrieve several more points.

2.6.3 Grounded Coplanar Waveguide

GCPWs are comprised of a central track separated from ground planes on both of its sides by small gaps along its length. Another ground plane found beneath the substrate characterizes the first G in GCPW. This ground plane pulls the remainng electric field lines that were not already coupled on the top ground planes. A drawing of a GCPW architecture can be seen on figure 13a. Grounded coplanar waveguides support wider

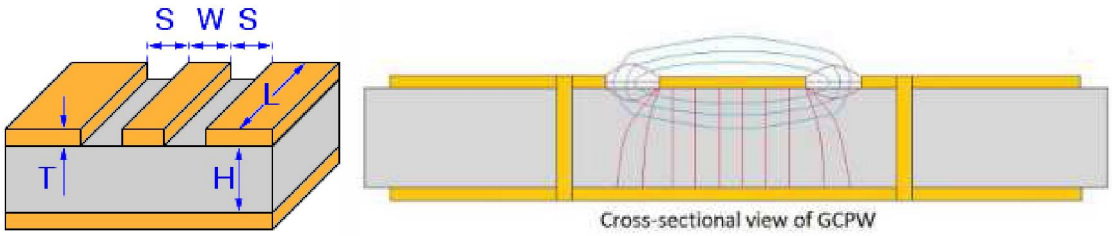

(a) GCPW architecture as seen on QUCS

(b) Cross-section of generated fields on a GCPW. Blue lines represent magnetic field lines. Red lines represent electric field lines. Yellow boxes represent copper or other conductor.

Figure 13 – GCPW cross-section layout

bandwidth than microstrips and are more suitable to higher frequency FMR acquisition. The measurements this work has achieved though, have shown very little differences, if at all, between the two. As the work of (MALORATSKY; LINES, 2000), GCPWs would only be necessary on frequencies beyond 28 GHz. GCPWs are less dispersive though and allow for lower effective dielectric constant variation as a function of frequency. GCPWs solve to narrower central tracks when compared to microstrips. This increases the proportion of the magnetic field generated above the waveguide which in turn makes more measurements in higher frequencies possible. They also radiate less and therefore have better field homogeneity along the waveguide. One may argue that most of these characteristics are circumvented by the mere application of the waveguide calibration in the VNA but calibration alone can not create useful measurement-wise bandwidth beyond physical limits. For instance, if a point high-up the frequency ladder does not generate enough magnetic field to magnetize the sample, calibration alone will not magically raise the reading resolution. An schematic of the fields generated by GCPWs can be seen on figure 13b.

3

Experimental Setup

3.0.1 Viability

A brief evaluation of the equipment's available capacity to perform VNA-FMR is discussed below.

As the most important piece of equipment in the VNA-FMR apparatus, the VNA used in this work is able to perform readings from 100 kHz to 18 GHz. Evaluating this capability under the hydrogen-electron's $\gamma \sim 42\, GHz/T$ one reaches the conclusion that the maximum useful external magnetic field will be of $\sim 430\, mT$. This field is completely attainable by the Power supply unit (PSU)/Coils system present in the apparatus. Another requirement for the FMR phenomena to happen within the material is that all of the electrons under testing be already beyond magnetization saturation, that is, all excited electrons will have their magnetic moments aligned. On this pre-state, any external field contributions to the sample's effective magnetization vector will cause the same orientation on every individual atoms' magnetic moment.

One of the samples tested under VNA-FMR in this work, permalloy, a ferromagnetic iron-nickel alloy notorious by its strong FMR signal, saturates magnetically at a few militeslas, thus, reaching testing-ability status.

The PSU/Coils system reached magnetic fields in excess of 1.2 T (only 990 mT annotated shown on figure 17b), so, it was completely able to provide the necessary external fields to cause precession on the sample's net-magnetization-carriers electrons. Two correlation graphs between the arduino's source signal, a 10-bit integer, and the corresponding generated H field are shown on figure 17. Fortuitously, In-Plane (IP) permalloy-sample/external-field layout usually requires just low fields of up to 430mT. Out Of plane (OOP) orientation commonly requires higher fields and one tested sample run out of field in this orientation even before 13 GHz. Even with OOP layout allowing for a distance between the cores of mere 5 mm as the waveguide was then orthogonal to the cores, it

was still not possible to reach the necessary fields, a consequence of an anisotropic field. Anyway, an arbitrary number of measurements, only limited by the apparatus overall resolution would be completely available.

As the magnetic field generated by the coils falls with an inverse factor of the square distance on a z-axial axis, the coils were positioned as near as possible beside the sample/waveguide set. A picture can be seen on figure 25 featuring a grounded coplanar waveguide (GCPW) waveguide with a permalloy sample on it. A simulation performed on femm (finite element methods magnetic) software shows the magnetic field between the cores to be homogeneous. In the very middle point between the cores the field shows a very shallow derivative. The simulation was modeled around a $1\,T$ field.

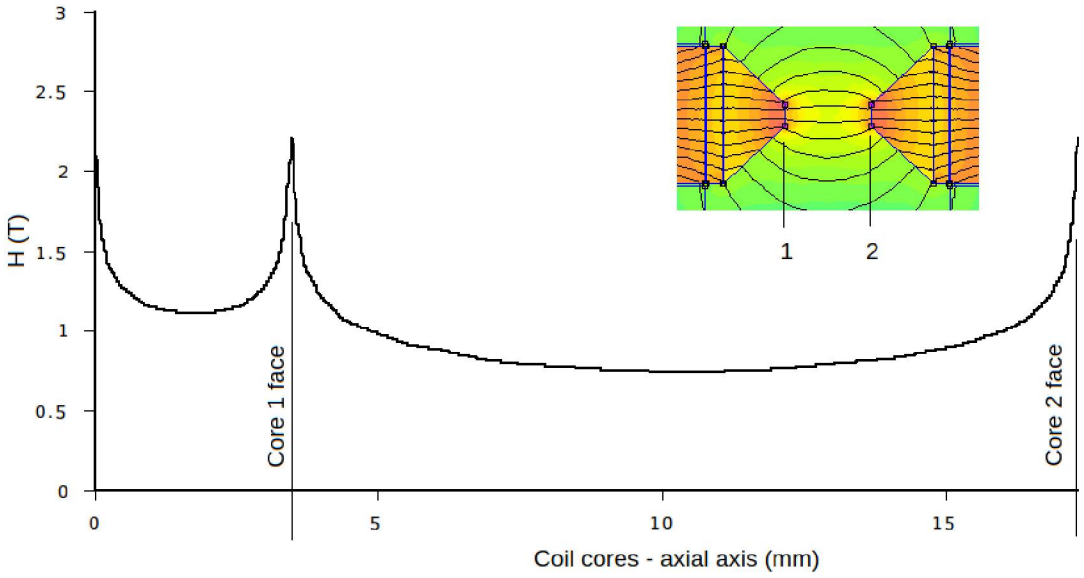

Figure 14 – Field homogeneity

The waveguides will be subjected to a $-0.5\,dBm$ power source from the VNA. That translates to 891 μW from

$$P_{mW} = 1\,mW 10^{PdBm/10}. \tag{3.1}$$

Equating $P_{mW}/(4\pi d^2)$ to the Poynting vector S, d a radial distance, one reaches:

$$\frac{P_{mW}}{4\pi d^2} = \frac{EB}{\mu_0} \tag{3.2}$$

Rewriting E as:

$$E = B\,.\,c \tag{3.3}$$

c being the light speed constant. One reaches:

$$\frac{P_{mW}}{4\pi d^2} = \frac{E^2}{\mu_0 c} \tag{3.4}$$

$$\frac{P_{mW}}{4\pi d^2} = \frac{B^2 c}{\mu_0} \tag{3.5}$$

$$B = \frac{1}{d}\sqrt{\frac{\mu_0 P}{4\pi c}} \tag{3.6}$$

Replacing variables with values one reaches the approximate B field $0.85\,\mu m$ (half the copper track thickness) from the conductor's center:

$$B = \frac{1}{0.85\,\mu m}\sqrt{\frac{4\pi\ 10^{-7}\ .\ 891\,\mu W}{4\pi\ .\ 3\ 10^{8}}} \tag{3.7}$$

$$B = 641\,\mu T \tag{3.8}$$

It is worth remembering that $B_{\mu_{Py}}$ field will vector-add to the external H field (now a B field within the sample) so that a spin precession establishes itself. $B_{\mu_{Py}}$ however is the I_{RF} generated field which pumps energy at the precession. Despite causing the precession, $B_{\mu_{Py}}$ addition to H field is negligible as it is several orders of magnitude smaller than it.

Finishing the viability analysis, a simple check with the Kittel fitting equation 2.21, returns:

$$f = \frac{\mu_B\, g}{h}\sqrt{H(H + M_{eff})} \tag{3.9}$$

$$f = \frac{9.27\ 10^{-24}\ 2}{6.06\ 10^{-34}}\sqrt{0.100(0.100 + 1)} \tag{3.10}$$

$$f = 10.1\,GHz \tag{3.11}$$

Experimental measurements (as seen on figure 28) show that this frequency is off by merely $1\,GHz$. Having in mind that h_{RF} calculation varies with distance, the conductor was considered cylindrical, and that the FMR phenomena will couple with P_{mW}, diminishing it a couple percentage points in the case of permalloy, the result is acceptable.

3.1 VNA-FMR

There were two major installments of this setup: a software synchronized one and a hardware (trigger) synchronized one. Both setups on the basis of H field sweeping and were able to analyze the sample in OOP and IP orientations. The second apparatus

however was able to achieve quite superior rates of data acquisition and was much more practical for investigating every FMR-related aspect of the samples.

A VNA-FMR apparatus needs to be self-compatible to be able to acquire any measurements. Most materials have γ values on the order of tens of GHz/T and so, it is necessary to have a coil system capable of generating a field γ-proportional to the maximum frequency the VNA is able to produce. As calculated for the graph on figure 6, $\gamma = 43.2\,GHz/T$ for a permalloy sample, $100\,nm$ thick. It is easy to see on the graph that H fields almost up to $300\,mT$ were necessary in order to reach the resonances lying in $18\,GHz$, the used VNA's maximum frequency.

The setup schematic shown on figure 15 represents the, so called, synchronized-field sweep, where the H field is controlled by the arduino via a current square signal fed into the PSU current channel amplifiers. Slightly different, the so called step-field sweep, commands the PSU to send specific currents to the coils via standard commands for programmable instruments (SCPI) language commands. As so, there are no cables connecting the arduino to the PSU and there is another data cable connecting the computer to the PSU.

The cables which connect the VNA's port A and B to the GCPW waveguide are RG-316 class, capable of carrying $18GHz$ signals with 74.6 % efficiency for a $30\,cm$ length. As they were used in this quite short length their losses did not amount to noticeable signal run-off. Some waveguides had the cables soldered straight to the waveguide main signal track and ground plane(s). This also did not prevent data acquisition. The GCPW milled in-house had female sub-miniature type A (SMA) connectors.

The red cables carry current from the arduino to the PSU, the square signal and from the computer to the arduino to feed the board itself with electricity. The brown cables transmit current to the coils, which are connected in series themselves to maximize the achievable H field. The probe is considered part of the gaussmeter and its cable will not be discussed as it specified by the manufacturer's own calculations. The gray cable connecting the VNA to the computer is an ethernet one through which it is able to receive SCPI commands and send data back to a serial monitor, in step-field sweep case, S_{21} transmission parameter values. In synchronized-field sweep, the whole VNA's $y = S_{21}(time)$ data array is available to be downloaded from the computer once the sweep is done. A synchronized-field sweep running 256 averages at the VNA typically takes $\sim 10\,s$ to finish.

The sample holder will stand amid an external homogeneous magnetic field generated by a twin-core BUCKLEY SYSTEMS LTD electromagnet driven by a remotely controllable KEPCO PSU (power supply unit) able to vary current up to $8\,A$ at $50\,V$. The VNA is a two port KEYSIGHT ENA-5063A able to sweep frequencies from 100 kHz up to 18 GHz . The gaussmeter is a PHYWE which can read fields up to 1.9 T. The

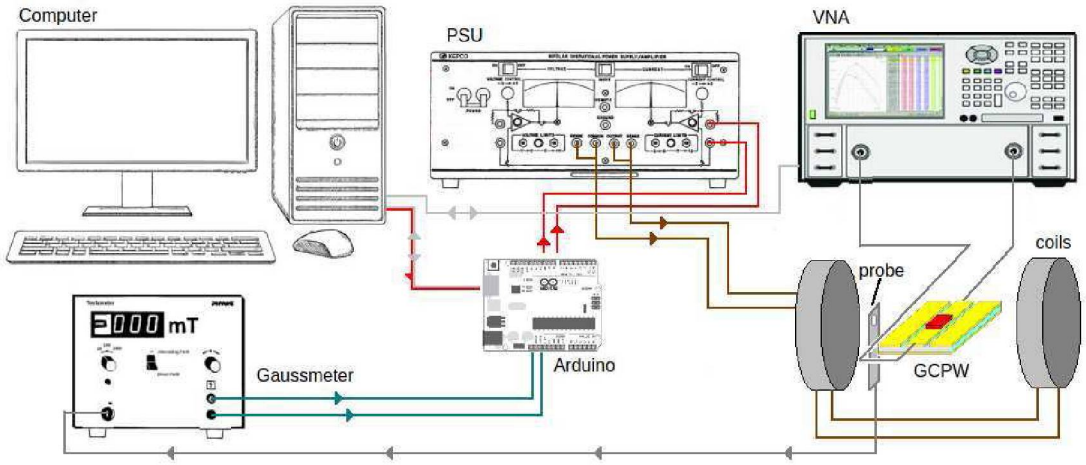

Figure 15 – Schematic of the VNA-FMR setup.

arduino is an Arduino-nano featuring an ATMEGA 168 processor. PC is a generic computer running windows 10, serial port monitor and Hot Keyboard macro programming language.

3.1.1 Software

The whole FMR apparatus is very sensitive and the VNA's measurements change even at a human-hand proximity. Touching the RF cables alone results in immediate S-parameters through calibration loss. So a computer-run software control system was deemed necessary. Most used command buttons on the VNA were then cloned to a software run in the PC. Additionally, useful commands were added to save the VNA's acquired FMR data to a flash drive previously connected to it. These features can be seen on figure 16 Also, for the apparatus's step-field sweep installment, H field first and last values were entered in the software since the arduino would loop through these values at a given increment. A frequency value box is there too, but there is no increment on it since this work relies only in field swept systems.

This is accomplished selecting a frequency, say 4 GHz on the VNA, specifying a DC field sweep, 40 to 80 mT for example, and acquiring S_{21} on the go. It is interesting to set the DC field sweep step to be on the order of a militesla so a better defined lorentzian might be retrieved. As the coils sweep an intended field interval, the arduino would simultaneously read field values from the gaussmeter and send this data back to the computer via a serial port. The VNA also sent its S_{21} data to the computer at the same rate and FMR graphs were then built in scientific graphing software.

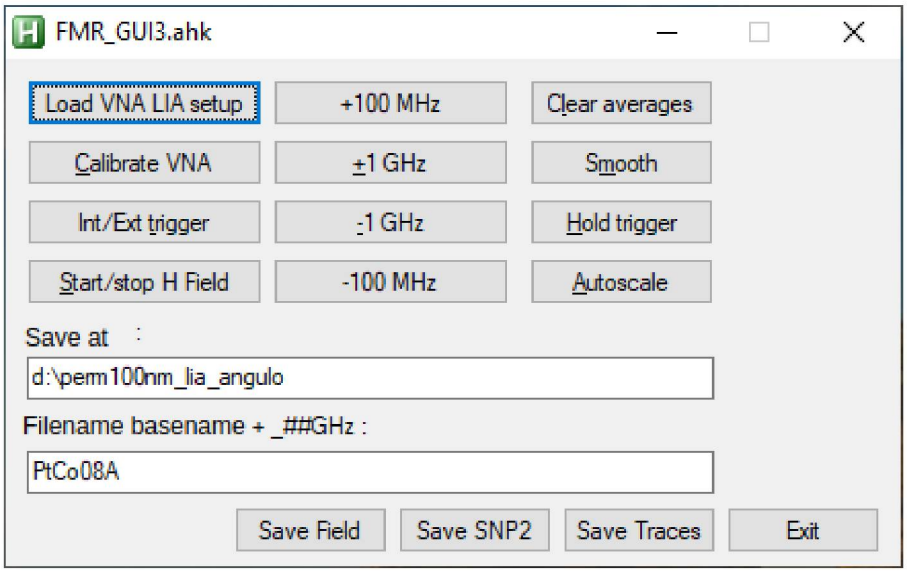

Figure 16 – VNA-FMR apparatus software control window.

3.1.2 Arduino

The arduino is the information hub in this setup. Its ability to easily interface with computer ports as well as its several analog inputs/outputs made it a very good solution for data interchange. It was set to send a square signal to the PSU which would then amplify these signals and drive the coils with the resulting current. The arduino version utilized, the Arduino-Nano, runs at a 20 MHz internal clock rate. All low-level software program processing happens at this rate or multiples of it. So, the fewer steps that there are in the program the more time is free for the arduino to process external data flow. Setting the square wave generation program in assembly, considered machine code essentially, it was possible to generate it at 20 Hz, of which only half was useful since readings only took place when the square triangle H field signal was going up. See figure 18.

3.1.3 Two VNA-FMR field sweeping techniques

As mentioned before, two main setup installments were used to obtain FMR data: a step DC field sweep and a synchronous DC field sweep, dubbed step-field sweep and synchronized-field sweep respectively. Synchronized-field sweep used the native signal generating capabilities of the arduino whereas step-field sweep issued SCPI commands to the PSU logically. VNA-FMR sweeps generate many data points and it becomes difficult to treat that data by hand. Its biggest advantage is exactly its ability to scan for resonances at as many frequencies as the experimenter wants. The more points, the

better the resolution. Based on this assertion, this work developed a second method of data acquisition, the synchronous-field sweep. This second measurement method was successful in achieving both easy-of-use handling and greater resolution capacity. On table 1 there is a comparison of both methods. The next two subsections describe in better detail these methods.

H Field Sweeping Techniques Comparison		
	Advantages/Disadvantages	
	Step-field sweep	Synchronized-field sweep
Points	50 points	200 points
Resolution	0.3 mT	0.1 mT
Sweep time	250 s	12.5 s
Visibility	Needs to be rendered on graphing software	Real time on VNA's screen
Hres finding	Time consuming trial and error	Easy finding by shifting field offset at the PSU
Data transfer	Each data stream (H field, S21) is separately handled and must be joined at graphing software	Time domain needs to be converted to H field
SNR	22.3 for permalloy	55.7 for Co25

Table 1 – Step-field sweep vs Synchronized-field sweep

3.1.4 Step-field Sweep

This apparatus took advantage of the PSU being controllable by SCPI language, so, a mixed language Autohotkey/SCPI program was built to issue the PSU a loop that sent current increments that traveled through the intended H field sweep for a given sample. The program was also tasked with receiving the Gaussmeter data and S_{21} data from the VNA. These incoming data were managed by two serial (one real and one simulated) ports, shown on the computer screen as two monitor windows. A third serial port monitor windows was also open for the PSU. The program controlled the data exchange in a step-field-wise way. So, it would send an incremented current value to the PSU and only then recover consequent S_{21} and H field values. This process took around 5 s for each data point. A hundred point lorentzian sweep would then take 8.3 minutes. It's also worth remembering that for unknown materials the first resonance point discovery rely on a lot of experimenting. This is to show that 8 minutes of sweeping added to several other minutes developing the associated graph looking for a resonance might easily run into some hours of investigation.

Both data, S_{21} parameter values and field values were synchronized via a macro software language on the PC. Both connections exist separately and the operator must

later blend the data sent to each of them on a single table and graph. It was possible to acquire the data in each of the sources at different rates if the end and start points were known. It would suffice then to interpolate the data of one of the sources to result in an equal number of points between both data streams. Another necessary step was to correlate the arduino sourced voltage signals and the gaussmeter magnetic field readings. As a linear correlation that it is, its graph returns intercepto-y (meant to be zero) and slope parameters that allow the operator to correctly configure these data on the software running on the arduino. In figure 17 one can see such correlation graphs. The arduino counts with a built-in low level PWM function. It is utilized to control the voltage level of its outputs and uses a maximum 12 bit integer number as argument. This will control the arduino's voltage out but the correlation graph is still necessary because the consequent H field between the coils depends on the distance between them. So, the graphs on figure 17 are basically a calibration of field values.

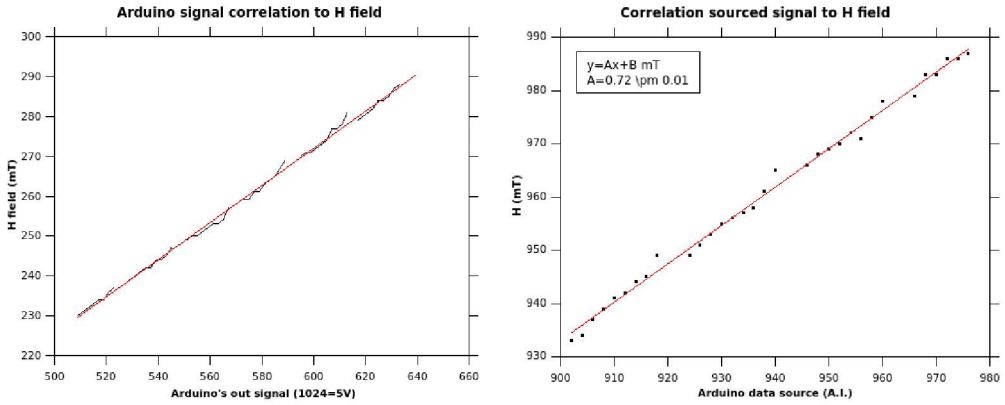

(a) Low-fields setup. Typically for IP layout.

(b) High-fields setup. Typically for OOP layout.

Figure 17 – H field correlation with an Arduino's 10-bit signal.

A retrieved resonance lorentzian for a permalloy, $100\,nm$ thick sample by the step-field sweep method is shown on figure 18. This dataset is 50 points long and took 4,17 minutes to acquire. A straight line was subtracted so the fitting lorentzian was upright.

Step-field sweep has achieved an $SNR = 24.3$ for the permalloy sample. A Savitsky-Golay fitting was applied to raw data and then the fitting was subtracted from the raw data in order to acquire the maximum variation from the average. The FMR signal peak was then divided by that maximum variation to achieve the SNR.

3.1.5 Synchronized-field Sweep

A second apparatus installment saw the arduino sending a voltage square signal to the PSU amplifier ports instead of controlling the PSU via SCPI from the computer.

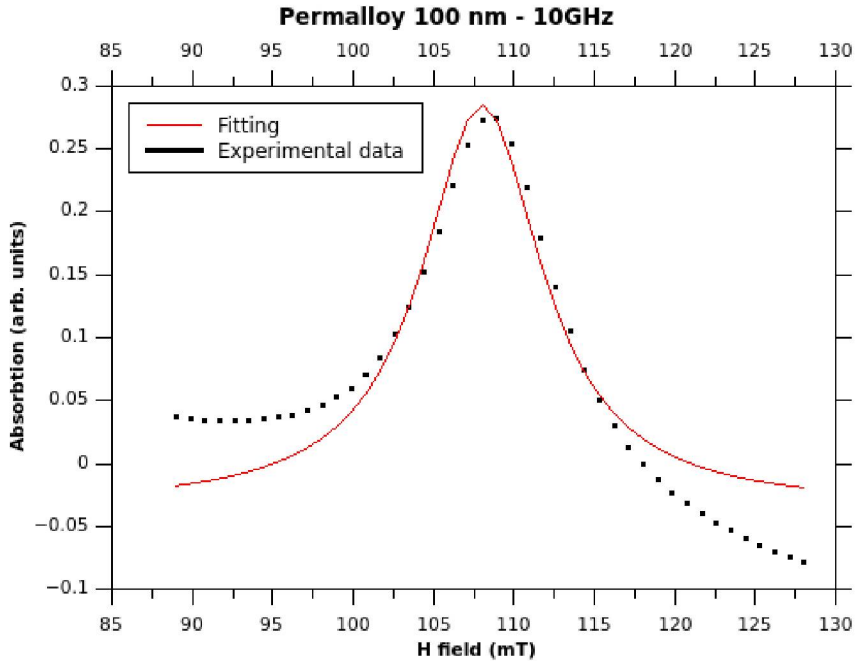

Figure 18 – Permalloy 100nm FMR at 10 GHz acquired with step-field sweep.

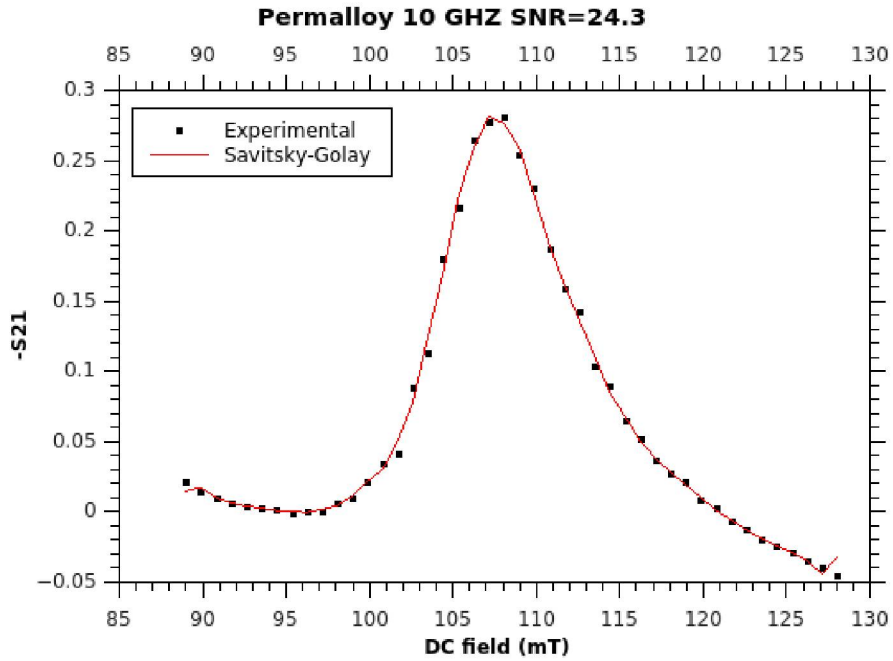

Figure 19 – Permalloy 100 nm IP orientation raw data fitted with Savitsky-Golay fitting algorithm. SNR calculated over this graph was of 24.3

Being a low-level approach to controlling the PSU, this attack at the problem allowed for

a greater rate of signal flow.

Dubbed synchronized-field sweep, this setup uses a square-wave generated by an Arduino to modulate the magnetic field applied to the sample. This square wave is then sent to both the PSU amplifier and the trigger input of the VNA. The frequency chosen for the square wave is 40 Hz, which is well adapted for generating a triangular shape current in the electromagnet, due to its inductive behavior that integrates over time the original square wave voltage. The same frequency is also convenient for triggering the VNA measurement, which takes about 50 ms to acquire 200 points. This is shown on the experimental graph on figure 20.

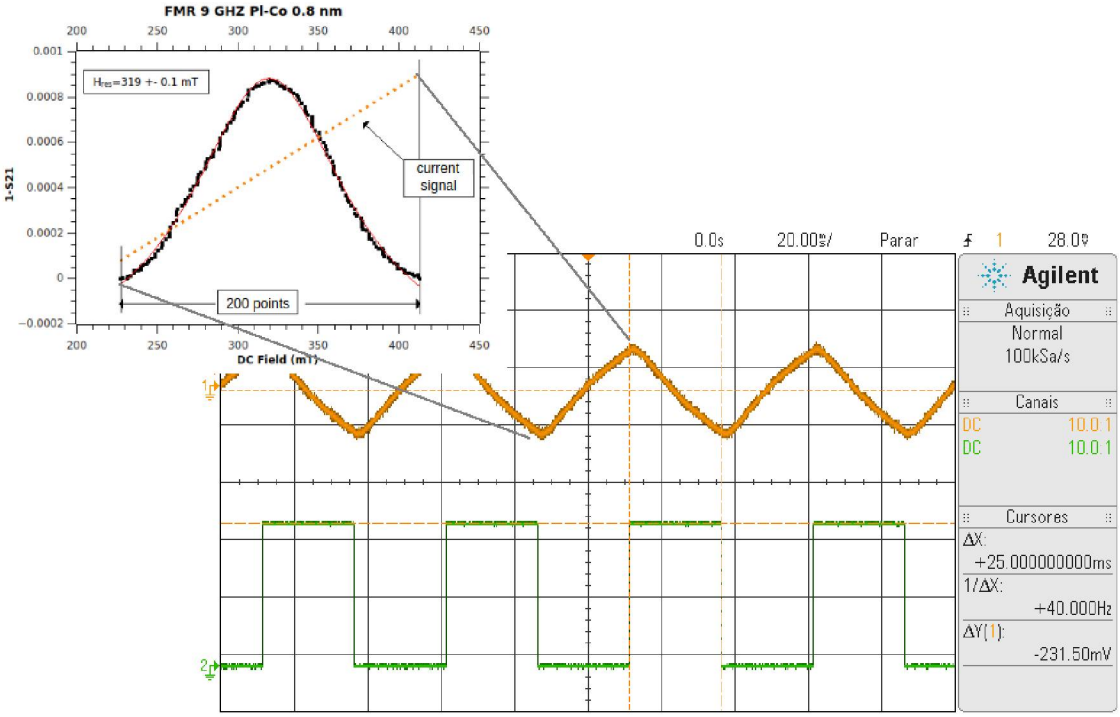

Figure 20 – Arduino generated square wave (green) and consequent H field (orange) measured between the coils as measured on an oscilloscope.

The VNA reading was synchronized with the square signal via a trigger down setting. This ensured that S_{21} readings would happen along the H field signal going exclusively up. Setting the VNA to show data in time-domain and making its sweep time equal to the square signal half-period had the VNA plot S_{21} values in real time. Specifying the VNA's number of averages to 256 resulted in a sweep time of 12.8 s if the square signal's period is of 50 ms. In the first apparatus this time would not be enough

to acquire 3 points, let alone 200, the quantity of points the VNA is able to sweep in this setup.

In this setup installment yet another hardware feature was added: a potentiometer trough which it was possible to control how much to amplify the arduino's signal. This is very useful when switching from large linewidth materials to narrow ones. Or to help look for the resonance in unknown materials. Of course, each time this amplifying factor was modified a new H field calibration, as the one on figure 17, had to performed.

A last feature of synchronized-field sweep, it has achieved an $SNR = 55.7$ for the $Co25\,nm$ sample. A Savitsky-Golay fitting was applied to raw data and then the fitting was subtracted from the raw data in order to acquire the maximum variation from the average. The FMR signal peak was then divided by that maximum variation to achieve the SNR.

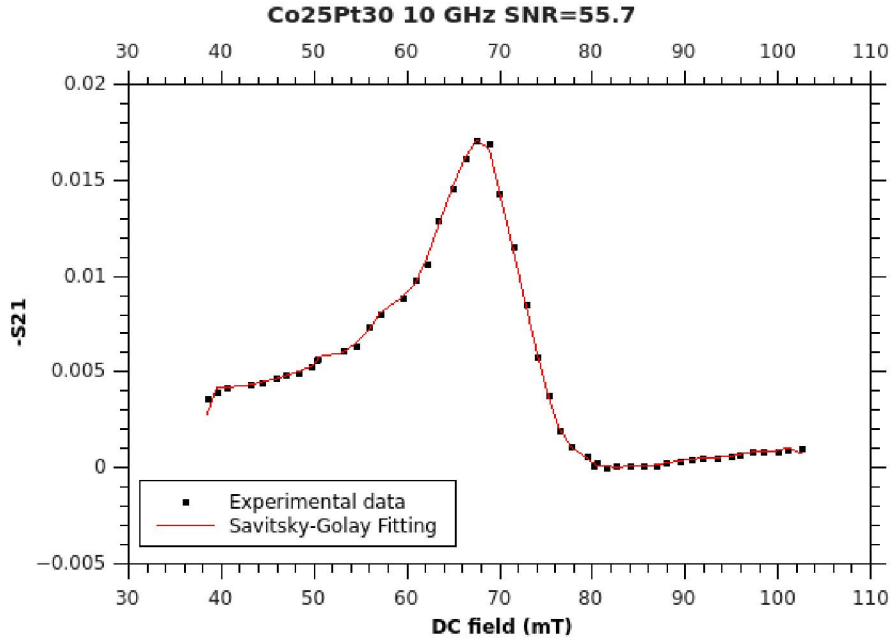

Figure 21 – Co25Pt30 IP orientation, acquired through synchronized-field sweep, raw data fitted with Savitsky-Golay fitting algorithm. SNR calculated over this graph was of 55.7

3.2 Waveguides

The sample holders manufactured for this work were actually "S" shaped or "U" shaped. For all of the VNA-FMR acquisition were utilized a total of three planar waveguides: 1 microstrips, 1 GCPW and 1 GCPW with metalized holes. Their actual charac-

teristic impedances might be calculated through the equations:

$$Z_0 = \sqrt{Z_{SC} Z_{OC}} \tag{3.12}$$

$$Z_{TL} = Z_S \frac{1 + S_{11}}{1 - S_{11}} \tag{3.13}$$

$$Z_{SC} = Z_{TL=SC} \tag{3.14}$$

$$Z_{OC} = Z_{TL=OC} \tag{3.15}$$

Where Z_0 is the characteristic real impedance of the transmission lines (TL); Z_S is 50 Ω; Z_{SC} is the frequency domain shorted circuit (SC) complex impedance; Z_{OC} is the frequency domain open circuit (OC) complex impedance; and S_{11} is the S reflection parameter.

The calculations for Z_{SC} and Z_{OC} were performed for GCPW1 and can be seen on figure 22. Z_{SC} and Z_{OC} are point-wise calculations of equation 3.13. Characteristic impedance Z_0 is an average real numbers array.

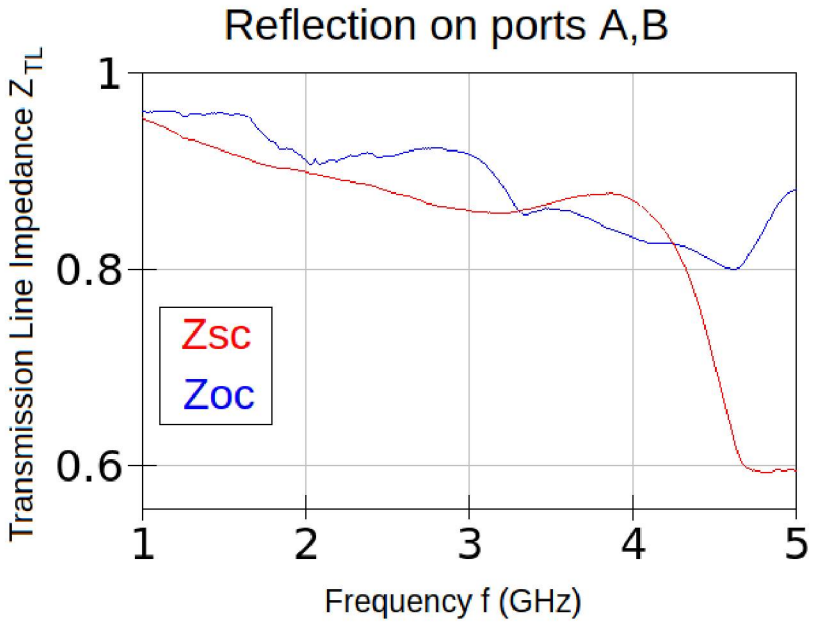

Figure 22 – GCPW transmission line impedance calculation on QUCS from experimental data captured on VNA.

Point-wise Z_0 calculations, performed against equation 3.12, are shown on figure 23. Impedance Z_0 is a real number. It has a mean value of 49.2 Ω, quite near the 50 Ω for which it was designed. Graphs on figures 22 and 23 were developed within QUCS and were calculated on a thousand points abscissas array. This waveguide was manufactured with soldered SMA connectors and so it was possible to evaluate it with short RF cables. Long cables, like the ones soldered directly to the other waveguides, carry too much weigh when averaging Z_0 and those analysis were not shown here then.

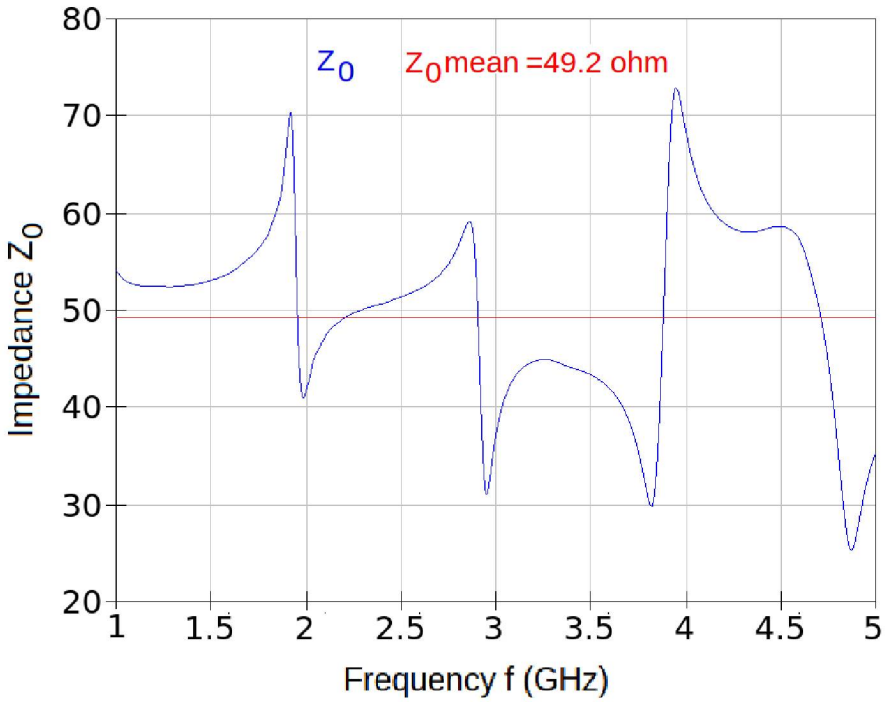

Figure 23 – GCPW transmission line impedance calculation on QUCS from experimental data captured on VNA.

These measurements were performed from 1 GHz to 5 GHz. RF capable cables are needed to carry the signal with low loss so that FMR signals stay viable. The cables were terminated with SMA connectors, known to hold signals with low loss up to 25 GHz, beyond the VNA capacity therefore.

A list characterizing the waveguides dimension is shown on table 2. Photos of them are shown on figure 24.

	Waveguide		
Dimension[1]	Microstrip	GCPW1	GCPW Thales
T	17.5 μm	17.5 μm	17.5 μm
W	1.87mm	1.70 mm	1.00 mm
H	965 μm	965 μm	965 μm
S	N/A	1.00 mm	1.00 mm
L	40 mm	40 mm	40 mm
Track shape	S	S	U

[1] See figures 12a and 13a

Table 2 – Waveguides dimensions

Mechanical stability is an important factor when acquiring FMR signals. Sample holders were securely anchored with plastic supports and brass screws. This was even more important for the synchronous acquisition setup when the field varies with a 33 Hz

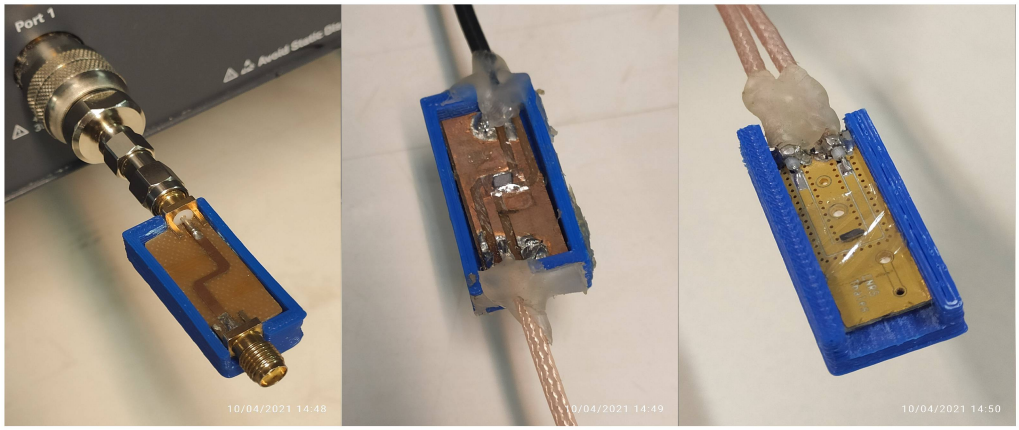

(a) Microstrip (b) GCPW1 (c) GCPW Thales

Figure 24 – Waveguides photos

frequency while swinging the magnetic field up to a half tesla, then, it becomes very easy to start a mechanical vibration from attraction to ferromagnetic parts. FMR depends on a small portion of the sample being magnetized homogeneously and coherently. Vibrations hinder that from happening. The sample itself, the sputtered film, is too light to pose such a problem. A picture of the GCPW with metallized holes with a sample on it between the coils is shown on figure 25. In this detail the sample (1 mm wide) fits completely inside the edges of the waveguide. Notice the brass screws. In this layout, IP, the external field lines are coplanar with the waveguide field lines. The sample must lay near the center of the coils, axially and radially to ensure it is in a Helmholtz volume between the coils. The coil and PSU setup utilized allowed for a maximum field of little more than a tesla. Greater fields were made possible by rearranging the coils to be in parallel voltage supply. That minimizes the resistance and maximizes current, the singular factor which most increases coil fields. Liquid cooling was also employed on the coils through tubes embedded in the coils. That also kept measurements repeatable over time since coil temperatures would not vary.

The samples, individualized on table 3, were all fabricated through sputtering with thickness varying from $0.8nm$ to $100nm$. They were positioned in flip-chip orientation. Conductive samples were either insulated from the waveguide with a PVC film or they were already terminated with an additional insulating layer, like 3 nm tantalum, sputtered last.

A GCPW layout was used but the literature tell us that for up to 18 GHz, microstrip and even stripline transmission technologies would have performed as well (COONROD; RAUTIO, 2012). S_{21} measurements were actually performed using an in-house microstrip solution and it worked just as well. Ours was machined out by a PCB-milling solution. Track width and/or separation from ground planes were calculated as

	Dimension				
Sample	Thickness	Width (mm)	Length (mm)	g-factor	α
Py	100nm	8	1	2.056	0.00735
CoPt	15/30nm	4	3	1.74	0.037
CoPt	8 Å/10 nm	4	3	1.95	0.023

Table 3 – Sample dimensions

the work of Maramis and Gupta (MARAMIS; J.; GUPTA, 1988). The microstrip devised was "S" shaped and, unlike the "U" shaped Thales-labs supplied GCPW, had its corners geometry calculated to keep impedance variation acceptable up to 18 GHz.

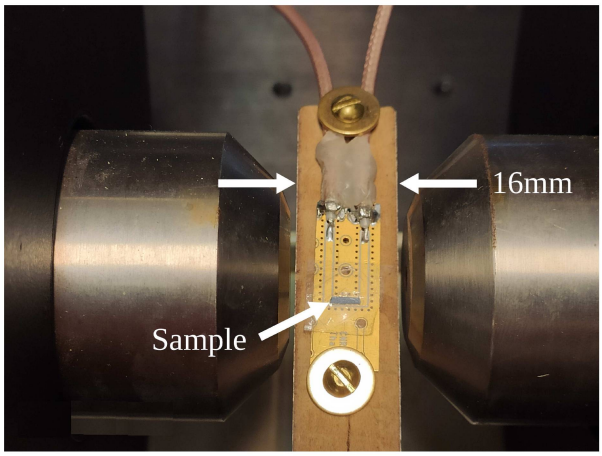

Figure 25 – GCPW Thales transmission line with a permalloy sample on top of it, inserted in the gap of an electromagnet. In order to get a homogeneous field, the sample must be centered to the electromagnet polar pieces. The maximum DC field obtained with this air gap is 0.6 T.

The IP (in plane) magnetic field orientation has been investigated, in which the magnetic field lines run parallel to the track section above which the sample is.

Another possible assembly is the OOP (out of plane) orientation, when magnetic field lines cross the PCB surface at an straight angle. These orientations result in different FMR data since nanothick-samples have an usual OOP shape anisotropy. The IP acquired data shows tha FMR signals for permalloy required considerably smaller external DC fields, a consequence of this magnetic soft axis.

A 2-port VNA through calibration was performed before every sweep. This calibration took place near the expected resonance field, predicted with common γ values.

Already during acquisitions, the VNA was through-calibrated with the sample holder and sample at an expected resonance field, predicted with common γ values. Based on the symmetry of FMR's behavior, this procedure would ensure higher observable peaks and lorentzian symmetry.

4

Results and Discussion

This work has made extensive use of the lorentzian bell curve to model mathematically the resonance point surroundings. The lorentzian was chosen over a gaussian distribution because its construction addressed closely the involved physical quantities: resonance frequency and H field. A lorentzian differential curve fitting was also readily available in the literature and was used specially for the retrieval of FWHM values, which themselves are variables for resonance linewidth.

The Kittel fitting most reliable variable return is M_S, the upper magnetization value at which the sample starts to show an asymptotic behavior in relation to magnetization. Its γ value is better retrieved calculating the derivative of the graph at desired points.

It is also possible to rewrite the Kittel fitting replacing γ by g-factor g. The spectroscopic free electron g value is of great interest to science as has been found experimentally to be equal to -2.00231930436256 (MARQUARDT; QUACK, 2020). Under the Kittel FMR fittings however, this value never shows because, by definition, FMR only happens if a precession movement is present. This very precession, which is caused by a transverse magnetic field, vector adds to the g-factor. Besides, the net magnetic momentum carrier electrons, despite being loosely bonded to their atom's cores, are not free electrons and as so, sport other g values.

It is interesting, at this point in the description, to see that the Kittel IP fitting strongly resembles the formula for angular momentum for the spin, leading one to believe Kittel never intended the g-factor in his model to be that of the free electron. The OOP orientation does not sport this similarity as the added fields are co-linear and, therefore, need not Pythagoras theorem to solve it.

A modified Kittel fitting is shown on the graph in figure 35. This modification adds the retrieval of an anisotropy field. A field that is dependent on orientation within the sample.

Resonance's linewidth retrieval was achieved either by 2.15's fitting equation or by FWHM retrieval by Qtiplot's fitting on lorentzian curves. Uncertainties were, as expected, higher the thinner the samples were. Still, all of them showed a clear linear relation with frequency. The smallest uncertainty, for Permalloy under IP orientation, was of ±6%, the biggest, for Cobalt 8Å under OOP, showed ±25%. The fitting of more points and the use of a 90% confidence interval would reduce these uncertainties. The latter sample's α measurements suffered considerably because measurements beyond 13 GHz retrieved no resonances, certainly a waveguide SNR impediment.

All acquired data were treated in QtiPlot (VASILIEF; GADIOU; FRANKE, 2008), a cross-platform scientific application for data analysis and visualization. Unsynchronized data were interpolated so there would be the same quantity of data points for both magnetic field and S_{21}. Resulting experimental curves, which actually showed transmission dips, were inverted so it would be possible to fit lorentzian curves on them. With field sweeps enacted for several frequencies it was then possible to achieve the Kittel fittings which returned g and M_{eff} values. The linewidths required the lorentzians to be in differential format so that equation 2.15 could be applied. This was all developed within Qtiplot which also returned uncertainty values. This linear fitting returned Gilbert's α and H_0, an anisotropy measurement.

The Kittel fitting is considerably faulty as both effective magnetization $Meff$ and the gyromagnetic ratio γ are coupled and as so, the Kittel fitting equation (see 2.21), admits multiple close enough solutions for these two physical quantities. Decomposing M_{eff} in its components M_s, M_{any}, etc, is necessary if one is to acquire more certainty over these values.

Planar waveguides offer a plethora of solutions that need to be further investigated. GCPW was a very good contender for microstrip but its version with metallized holes showed much less deviation from standard 50 Ω impedance values.

An arduino microcontroller, a six dollar board, often downplayed, was a very good solution to reach higher resolutions in measurements through multiple field readings and measurements averaging. It was not, however, without high quality programming that this was achieved. Several lines of code were rewritten or extinct in order to save milliseconds from each loop of code and, in doing so, being able to exploit more averages per reading.

Another cheap player in this setup was the interpreted macro programming language: AutoHotkey (MALLETT; GRAY, 2009). Although not without its quirks, this automation environment allowed the creation of a whole interface to control the VNA, the PSU and the arduino all at once. All signals were saved from its interface as well.

The Lorentzian fitting approach proved very good but not without its quirks too. It was not expected for the lorentzian to show different approaching and departing plateaus

levels off its base. As a first attack at the problem, these curves were reacquired with a calibration performed at their resonant fields as it was theorized this unbalance could be the effect of unbalanced fields. This resulted in little, if any, difference. Signal acquisition drifting played a factor in most of the lorentzians. If left uncorrected they would introduce small additions to FWHM values, on the order of 35%. If they were equally applied to all measurements it would characterize a systematic measurement error. Curiously it would not affect then the calculation of the Gilbert attenuation coefficient but it would point to a mistaken H_0 value (see equation 2.23).

Measurements showed great repeatability. Synchronous setup was very practical to work with, since the team's first efforts to retrieve signals, time-to-graph has shrink from an hour to an instant, FMR signals actually are now shown on VNA's screen in real-time and with increased resolution.

4.1 Permalloy 100nm

Permalloy saturates at a few militesla and so shows FMR signals since 4 GHz. Because of this it was chosen as a benchmark material to the apparatus. The retrieved physical quantities closely comply with the literature (NIBARGER et al., 2003). These measurements were made under IP configuration, with GCPW1 sample-holder/waveguide. This sample was obtained through sputtering of permalloy material on a silicon substrate and later finished with a 3 nm thick tantalum layer. The sample itself was 1 mm wide and 8 mm long so that it fitted completely inside the waveguide track dimensions.

The lorentzian fitting algorithm used was the one referenced in equation 2.15 in conjunction with Qtiplot.

The graph on figure 26 is a typical example of single frequency field sweep, FMR signal acquisition. Black dots represent experimental data, red continuous line represents the lorentzian fitting as FMR is handled as a continuous signal. The dashed blue line is the derivative of the FMR signal on which equation 2.15 works on. The blue diamond shapes on it are the mathematically retrieved extremes of linewidth. These points were also projected on the lorentzian curve so to verify their symmetry. The pink triangle shapes localize the resonance field. Under step-field sweep acquisition technique only 50 field points were investigated for S_{21} signals. A good part of these points were already outside the lorentzian but nonetheless the curve end up well represented.

On figure 27 all of the retrieved FMR curves obtained for this sample under step-field sweep were plotted against their frequency. The peaks tendency to increase are caused by the Zeeman-effect energy being linearly proportionate to the frequency as shown on equation 2.2 and the graph on figure 4. With frequency change, however, also other

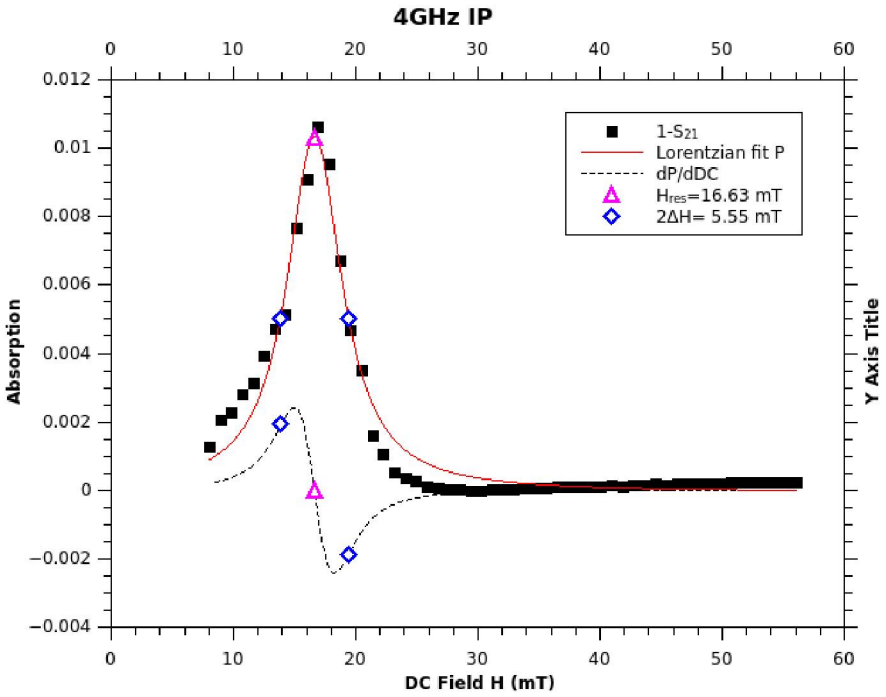

Figure 26 – Permalloy 100 nm thick sample. Lorentzian fitted FMR resonance at 4 GHz under IP orientation. Data acquired with step-field sweep technique. See section 3.1.4.

effects take place, like radiated EM waves and then the available power to cause FMR decreases. Still, every investigated frequency returned some signal. This non-linear increase of peaks' height will affect adversely α determination as FWHM will not increase smoothly. This effect however, will have no consequence in the Kittel fitting as it relies only the peaks frequency position.

On the graph in figure 28 it is shown the Kittel fitting, introduced by Charles Kittel in (KITTEL, 1948). The g-factor returned by this fitting includes not only the electron's own but also orbital and contributions, hence its variation from the free electron $g = 2.0023$ (ODOM et al., 2006). The achieved fitting shown is a close match to (NIBARGER et al., 2003). Other works claim having achieved smaller uncertainties through proposed algorithms.

The Gilbert attenuation coefficient, certainly the most sought after physical quantity in FMR experiments as of now, was clearly retrieved on graph from figure 29. Its value, $\alpha = 0.00735$ for a 100 nm thick sample, is extrapolable from (ZHAO et al., 2016) and (NIBARGER et al., 2003) on table 4. This coefficient, typically identified by the greek letter α, is a phenomenological coefficient, its physical source (there might be more than one source) is not completely known. As mentioned earlier, different peak heights would affect diversely FWHM. However, the uncertainty kept itself to 4.5 parts per 73.5,

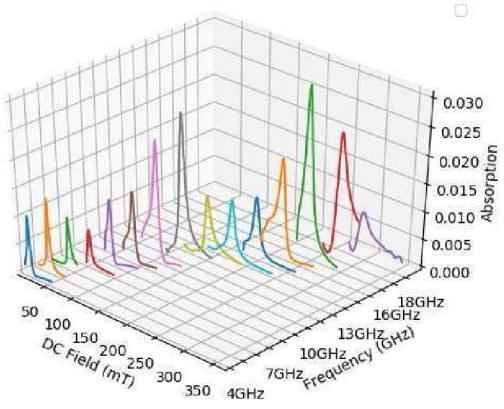

Figure 27 – Permalloy 100 nm thick sample. Fitted FMR signals for frequencies from 3 to 18 GHz.

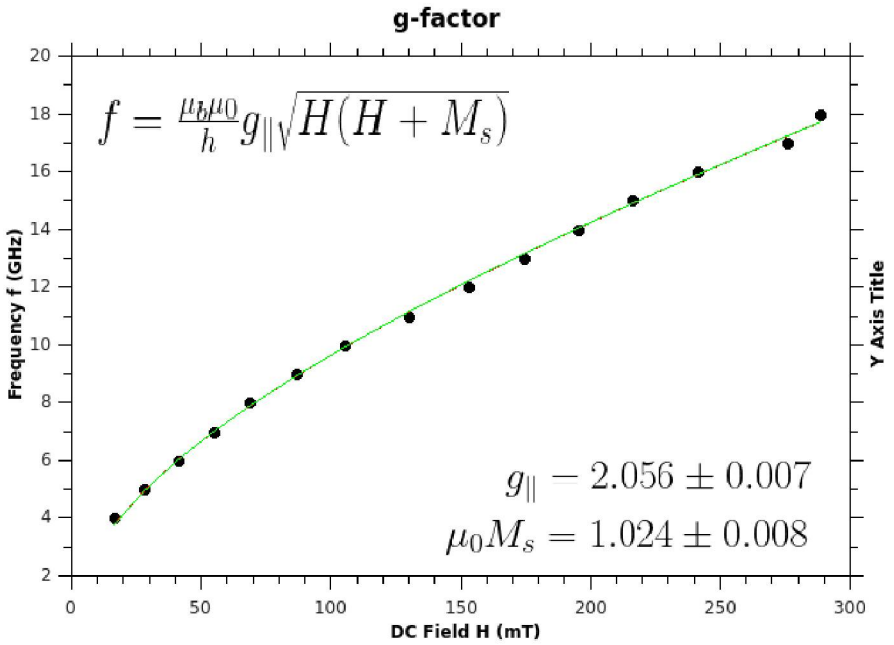

Figure 28 – Permalloy 100 nm. Kittel fitting. IP orientation.

$\sim 6\%$. Certainly a higher resolution is possible with this permalloy sample.

4.2 Platinum-Cobalt $25\,nm$

This was a Cobalt $25\,nm$, Platinum $30\,nm$, Titanium seedlayer with a alumina substrate. Cobalt is one of the three, room temperature, natural ferromagnetic elements.

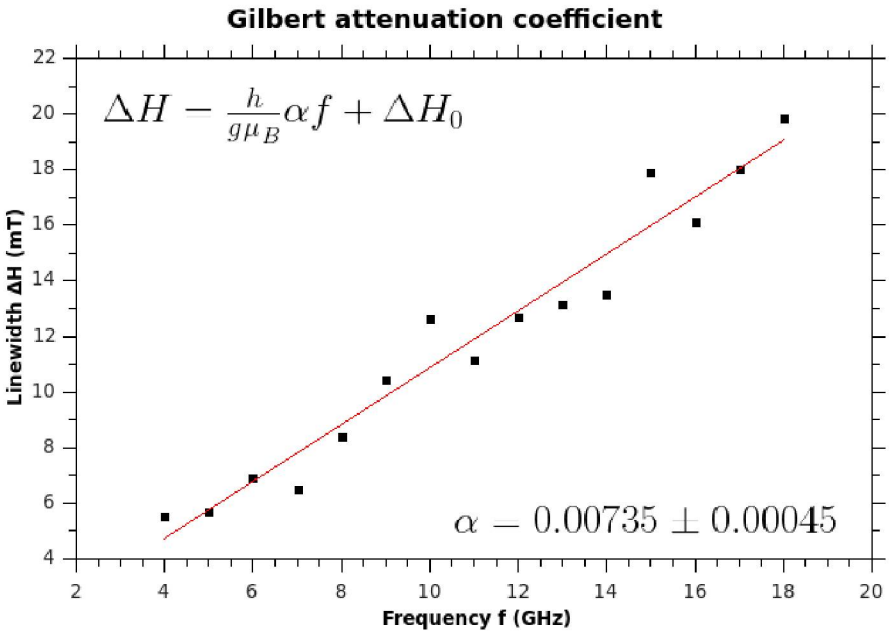

Figure 29 – Permalloy 100 nm. IP orientation. Gilbert attenuation coefficient α

Table 4 – Literature comparison

	Permalloy sample $Fe_{80}Ni_{20}$	
Feature	***Nibarger 100*** nm^a	***This work 100 nm***
M_s(T)	$1.00 < M_s < 1.08$	$1.016 < M_s < 1.032$
factor-g	$2.02 < g < 2.12$	$2.049 < g < 2.063$
α(e-3)	7.5	$6.90 < \alpha < 7.80$

[a]Extrapolated.

The other two being iron and nickel. As so, it has been a natural subject to FMR investigation and was also elicited for the apparatus here presented. This sample was submitted to be analyzed by another department and therefore it was decided to keep it whole. Its width was 5 mm , wider than the GCPW central track width. This required the use of a consumer-grade plastic wrap to prevent the sample from short-circuiting the waveguide and therefore, killing any FMR signal.

On figure 30 it is presented a typical FMR signal for this sample at $10\,GHz$. This sample's FMR signals were performed under synchronized-field sweep technique. The graph on figure 30 is presented with 88 abscissa points. If the sweep frequency could be increased there could be more points experimental points on the lorentzian itself. One can see that roughly half of the H field sweeping points, those after $100\,mT$, are of no interest to determine g-factor or α. This can be achieved by decreasing the PSU amplification of the arduino's square signal. Then, a 200 point sweep allocated to a 100 H field points

would increase the raw abscissa resolution to $0.5\,mT$.

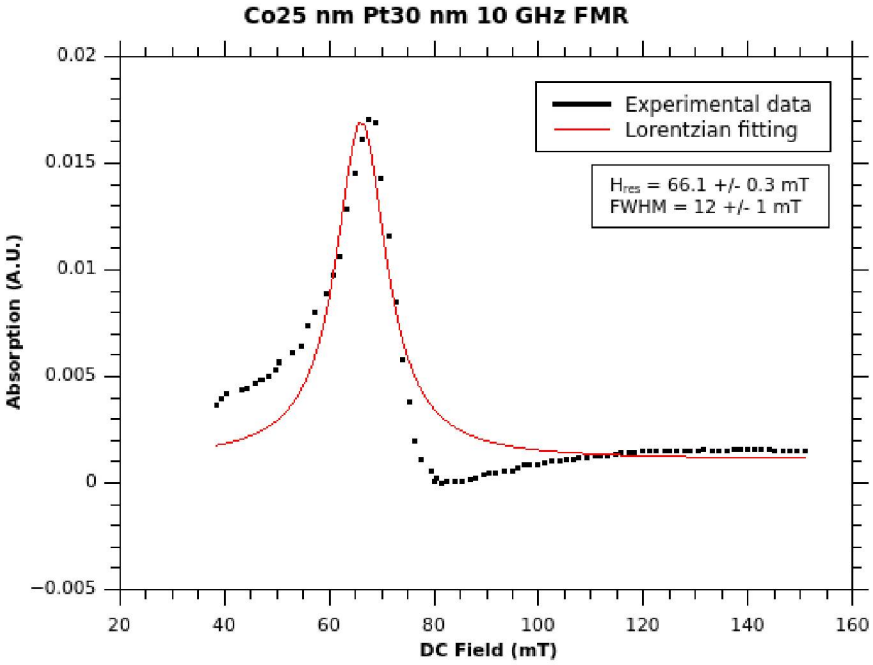

Figure 30 – Cobalt 25 nm, Platinum 30 nm. Lorentzian fitted FMR resonance at 10 GHz under IP orientation. Synchronized-field sweep acquisition. See section 3.1.5

Its Kittel fitting found a g-factor of 1.74, well below the g-factor for a free electron of 2.0023.

The α coefficient, fitted on graph in figure 32 retrieved with a 5 parts uncertainty per 37 nominal value, a 14% error margin.

4.3 Platinum Cobalt 8Å

This was a Cobalt 8Å, Platinum $10\,nm$, Titanium seedlayer with a glass substrate. On figure 33 one can see a typical FMR sweep at $9\,GHz$ of this sample. This sweep was performed at full 200 points retrieved a signal of less than 1 part per thousand. Uncertainty was kept under $0.1mT$ for the resonance, 1 part per three thousand. This particular resonant frequency along the $13GHz$ and $4GHz$ ones showed their linewidths considerably below average as seen on figure 36. This sample returned quite wide linewidths overall if compared to permalloy samples, see figure 29. This sample was also analyzed with the synchronous-field sweep technique. These lorentzians were fitted with the built-in algorithm of Qtiplot. They were however subtracted of a baseline to render the ascending and descending curves symmetrical.

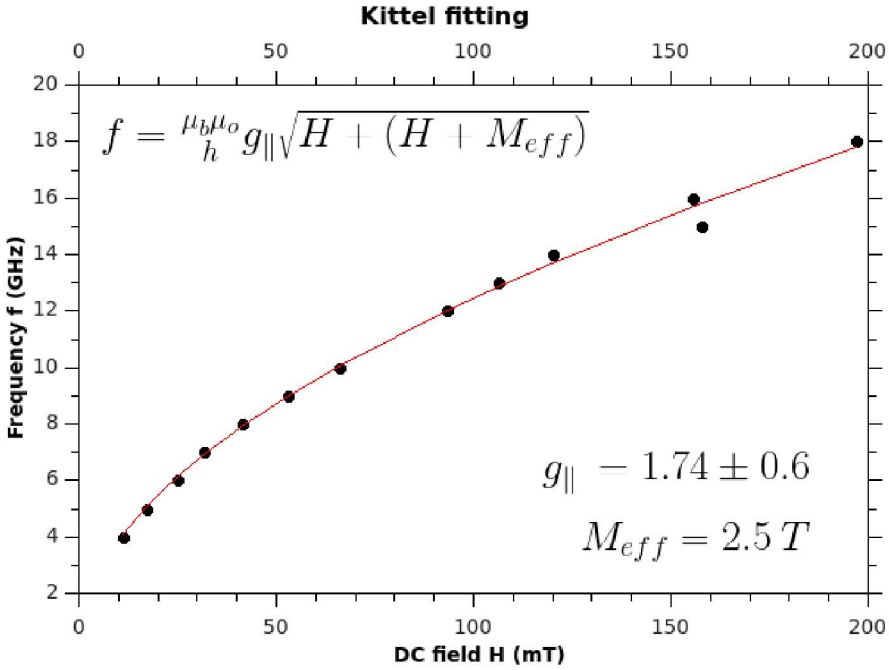

Figure 31 – Cobalt 25 nm, Platinum 30 nm. IP Kittel fitting.

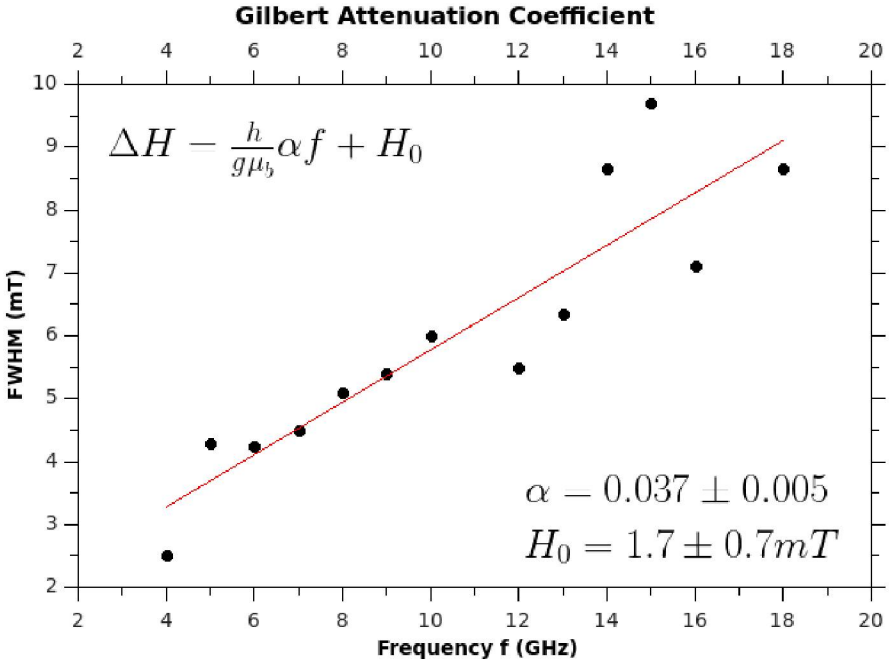

Figure 32 – Cobalt 25 nm, Platinum 30 nm. Gilbert attenuation coefficient α.

The black (200 in each curve) dots on figure 34 are experimental data. The colored continuous lines are fittings. Only GCPW1 was able to retrieve data from this sample and only up to 13 GHz as is shown. Further frequencies retrieved no FMR data data beyond above noise level. Given the large linewidths observed it became necessary to modify the

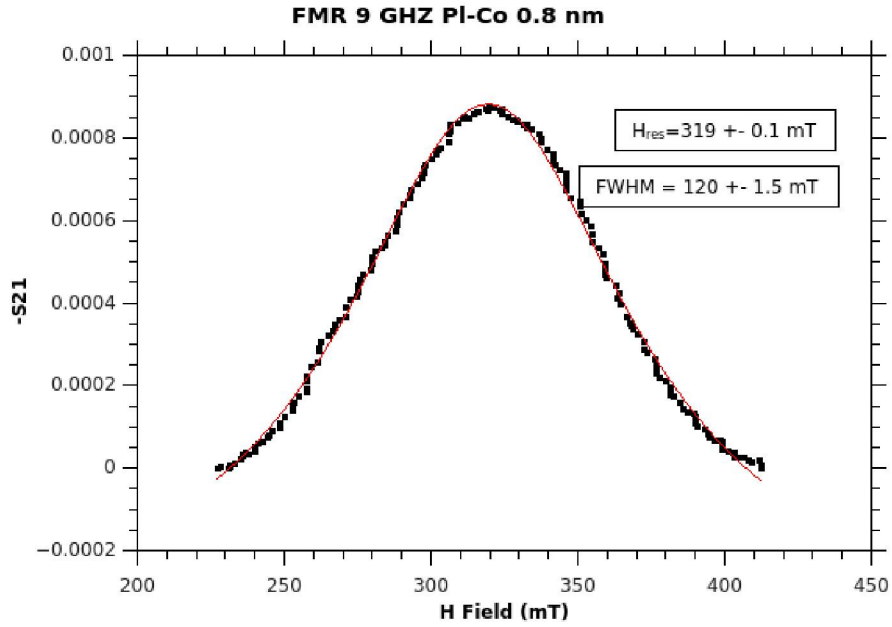

Figure 33 – Cobalt 8Å, Platinum 10 nm. Lorentzian fitted 9 GHz FMR under OOP orientation. Synchronized-field sweep acquisition.

H field sweep range for every frequency.

The steady increase in peak height of the resonances on graph in figure 34 is a consequence of the Zeeman effect whose energy increases linearly with the resonant frequency. It is relevant to remember however that there are non-linear radiating losses throughout the spectra, hence the inhomogeneity of the 13 GHz resonance point.

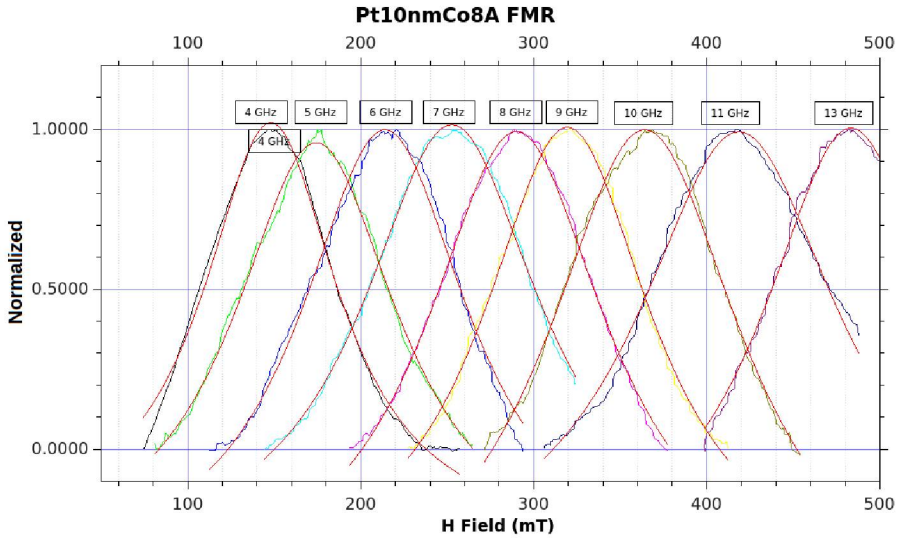

Figure 34 – Cobalt 8Å, Platinum 10 nm. Lorentzian fitted FMR resonances under OOP orientation. Synchronized-field sweep acquisition.

This setup was not able to capture resonances beyond the $13\,GHz$ frequency. It is possible that this is due to the fact that the signal carrier track, which is "S" shaped, might have a radiating resonance in its middle segment. This segment is around $8\,mm$ long and possibly houses half a period of a $13.5\,GHz$ standing wave. This radiating power would not be enough to hide Permalloy signals, which were shown to be as strong as 2.5 parts per hundred, but CoÅPt10nm showed much subtler signals of 2 per thousand.

In the graph on figure 35 it was introduced a new fitting variable in the Kittel fitting, an anisotropy field which was successfully retrieved by Qtiplot's algorithm. This setup actually used OOP (out of plane) orientation, when external magnetic field lines cross the sample at a perpendicular angle with its surface. Hence the equation used in the fitting, shown on graph in figure 35, is a derivation of equation 2.21. Uncertainty of α coefficient was up to a quarter of the nominal α value, which was itself three times as big as the permalloy sample tested in this work. small and linear correlation between linewidth and frequency was clear on graph in figure 36.

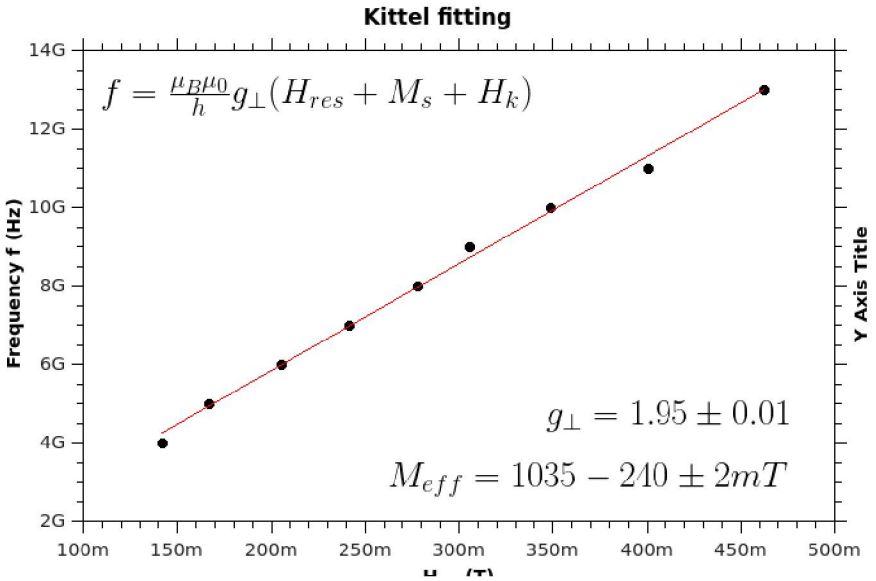

Figure 35 – Cobalt 8Å, Platinum 10 nm. OOP Kittel fitting.

Uncertainty of α coefficient was up to a fourth of the nominal α value, which was itself three times as big as the permalloy sample tested in this work. Were it not for the 4, 9, and $13\,GHz$ frequencies values α's uncertainty would be much smaller than the value seen on figure 36.

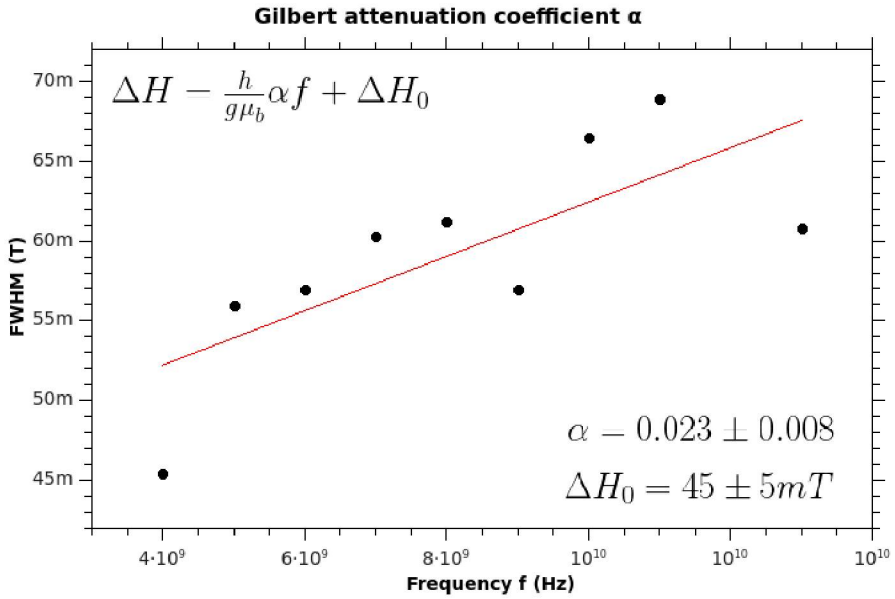

Figure 36 – Cobalt 8Å, Platinum 10 nm thick sample. OOP orientation. Gilbert attenuation coefficient α.

5

Conclusions

In this work we have successfully developed a VNA based FMR setup, using a broadband GCPW as the excitation and sensing device. We have used the transmission coefficient (S_{21}) given by the VNA, as the signal to analyze the RF absorption of the sample at the resonance frequencies. The setup is well adapted for thin film ferromagnetic samples characterization, giving information like Gilbert attenuation coefficient, Gyromagnetic ratio, g-factor and so on. Two approaches of the same setup were explored in this work, in order to compare and improve acquisition speed and SNR. The first approach, named step-field sweep, relied on discrete, sequentially acquired 50 field points, each one associated with S_{21} measurements along a probable FMR resonance. The operator would set in the software the initial, final and step field sweep values. The computer based software takes measurements of the S_{21} at each field iteration. Field values are measured using an analog Hall probe gaussmeter, which are converted to digital values by an Arduino. This approach was quite time consuming (around 15 min to make a graph with a single FMR curve) and resulted in a SNR of 24. The second approach, named synchronized-field sweep, is based on a fast magnetic field signal synchronized with the VNA measurement, so one can get an entire FMR spectrum in a fraction of a second (around 0.12 s). The synchronization is achieved by using a square wave, generated by the Arduino, that starts the sweep field together with the S_{21} measurement, taken with the VNA in zero span mode. Each VNA measurement is composed of 201 points, which were then averaged 500 times to increase the SNR. The field intensity and sweep amplitude are chosen so as to have an entire FMR lorentzian resonance curve within the VNA screen. As doing so, the user can easily see the formation of the FMR curve directly on the VNA screen. This approach proved to be much faster than the step-field sweep (around 2 min to make a graph with a single FMR curve) and resulted in a SNR of 55.

FMR signals were recovered from various thin film samples, as a Permalloy 100nm, a Cobalt25nm/Platinum30nm and a Cobalt0.8nm/Platinum10nm. The Gilbert attenuation coefficient was also calculated from them. The synchronous sweep approach proved

to be more practical as it yielded a higher resolution in readings and showed smoother graphs.

Successful retrieval of FMR signals even from sub-nanometer films, proved that the synchronized-field sweep approach is a successful technique compared to the traditional approaches. Permalloy thin film samples returned FMR signals at all available (18GHz) frequencies either in IP or OOP orientations. An extensive work has been done on the subject of g-factor as a function of thickness by (NIBARGER et al., 2003) and this work's numbers fitted that work very well, as we have shown in table 4.

FMR lorentzian fittings were thoroughly achieved whenever a peak curve was acquired. Resonance fields H_{res} were adjusted on Kittel fittings with little uncertainties while FWHM linewidths showed larger mean errors. These linewidth errors have a direct impact on Gilbert's parameter, which is discovered from the linewidths fitting. The g-factor, α, γ and M_{eff}'s returned values were completely consonant with the literature for permalloy.

5.1 Future developments

Other waveguides which better couple I_{RF} generated fields would be interesting to test. Waveguides designs that retain complex impedance close to Z_0 at high frequencies are crucial to keep the sample's FMR signals above noise level. This is especially true for ultra-thin samples like the Cobalt 8Å tested in this work which returned typically a 1/1000 parts signal. The best way to develop this is through EM simulation software like ADS and Sonnet, that are able to deal with dielectric constant and losses, which change with the excitation frequency. Besides that, better PCB materials and RF cables, would lend to better impedance match and lower dielectric absorption throughout the entire interest frequency span (1- 18 GHz). Another improvement would be a rotating sample holder, so as to further investigate anisotropy fields within the sample, which are of interest in the design of spintronic magnetic devices. Other interesting improvements would be a heating/cooling system that allows for the evaluation of the FMR signal as a function of temperature (possibly utilizing a Peltier) and an RF amplifier to source the GCPW with a higher RF field, allowing to evaluate the sample's non-linear response.

REFERENCES

AHARONI, A. et al. *Introduction to the Theory of Ferromagnetism.* [S.l.]: Clarendon Press, 2000. v. 109.

AKERMAN, J. J. et al. *Europhys. Lett.*, v. 63, n. 104, 2003.

ARKADIEW, W. *Annalen Der Physik. (in german)*, v. 2, 1923.

BARATI, E. et al. Calculation of gilbert damping in ferromagnetic films. In: EDP SCIENCES. *EPJ Web of Conferences*. [S.l.], 2013. v. 40, p. 18003.

BELEVITCH, V. *Thesis.* [S.l.]: Université Catholique de Louvain, 1945.

BRINSON, M.; JAHN, S. Qucs: A gpl software package for circuit simulation, compact device modelling and circuit macromodelling from dc to rf and beyond. *International Journal of Numerical Modelling: Electronic Networks, Devices and Fields*, Wiley Online Library, v. 22, n. 4, p. 297–319, 2009.

BUSCHOW, K. H. J.; BOER, F. R. et al. *Physics of magnetism and magnetic materials.* [S.l.]: Springer, 2003. v. 7.

CARDIAS, R. et al. The bethe-slater curve revisited; new insights from electronic structure theory. *Scientific reports*, Nature Publishing Group, v. 7, n. 1, p. 1–11, 2017.

CHAMBERS, S. A. A potential role in spintronics. *Materials Today*, Elsevier, v. 5, n. 4, p. 34–39, 2002.

CHAUDHARY, V.; RAMANUJAN, R. Magnetocaloric properties of fe-ni-cr nanoparticles for active cooling. *Scientific reports*, Nature Publishing Group, v. 6, n. 1, p. 1–9, 2016.

CHO, J.; GOODSON, K. E. Cool electronics. *Nature materials*, Nature Publishing Group, v. 14, n. 2, p. 136–137, 2015.

COONROD, J.; RAUTIO, B. Comparing microstrip and cpw performance. *Microwave Journal*, Horizon House Publications, Inc., 685 Canton Street Norwood MA 02062 United ..., v. 55, n. 7, p. 74–86, 2012.

CORTÉS-ORTUÑO, D. et al. Proposal for a micromagnetic standard problem for materials with dzyaloshinskii–moriya interaction. *New Journal of Physics*, IOP Publishing, v. 20, n. 11, p. 113015, 2018.

DARTORA, C.; CABRERA, G. *Phys. Rev. B*, v. 78, n. 012403, 2008.

DARTORA, C. A.; CABRERA, G. G. *Phys. Lett. A*, v. 334, n. 46, 2005.

DIETL, T. et al. *Spintronics*. [S.l.]: Academic Press, 2009. v. 82. 34–39 p.

DORFMANN, J. *Zeitschrift für Physik. (in German)*, v. 1, n. 98, 1923.

E., . N. R. *Modern Physical Metallurgy (Eighth Edition)*: Diamagnetism and paramagnetism, 8.6.2. [S.l.]: Elsevier, 2014.

FANG, D. et al. Spin–orbit-driven ferromagnetic resonance. *Nature nanotechnology*, Nature Publishing Group, v. 6, n. 7, p. 413–417, 2011.

FISCHBACHER, T. et al. A systematic approach to multiphysics extensions of finite-element-based micromagnetic simulations: Nmag. *IEEE Transactions on Magnetics*, v. 43, n. 6, p. 2896–2898, 2007.

FLOVIK, V. *Magnetization dynamics in nanostructures*. Tese (Doutorado), 2016.

FLOVIK, V. et al. Thickness and temperature dependence of the magnetodynamic damping of pulsed laser deposited la0. 7sr0. 3mno3 on (111)-oriented srtio3. *Journal of Magnetism and Magnetic Materials*, Elsevier, v. 420, p. 280–284, 2016.

G. G. Cabrera and N. Garcia. *Appl. Phys. Lett.*, v. 80, n. 1782, 2002.

GILBERT, T. *Physical Review*, v. 100, n. 1243, 1955.

GILBERT, T. L. A phenomenological theory of damping in ferromagnetic materials. *IEEE transactions on magnetics*, IEEE, v. 40, n. 6, p. 3443–3449, 2004.

GLADKOV, S.; BOGDANOVA, S. *J. Magn. Magn. Mat.*, v. 368, n. 324, 2014.

GREINER, W.; REINHARDT, J. *Field Quantization*. [S.l.]: Springer Publishing), chapter 8.2, 1996.

GRIFFITHS, J. *Nature*, v. 158, n. 670, 1946.

GRINSTEIN, G.; KOCH, R. H. *Phys. Rev. Lett.*, v. 90, n. 207201, 203.

GUIMARãES, A. P. *Revista Brasileira de Ensino de Física*, v. 22.3, n. 360, 2000.

HECK, C. *Magnetic materials and their applications*. [S.l.]: Elsevier, 2013.

HUBER, A.; SCHÄFER, R. *Magnetic Domains: The Analysis of Magnetic Microstructures*. [S.l.]: Berlin: Springer-Verlag, 1998.

JENSEN, E. Cavity basics. *arXiv preprint arXiv:1201.3202*, 2012.

JOOS, V. *Int. J. Circ. Theor. Appl.*, v. 28, n. 429, 2000.

KAHN, O. *Introduction to molecular magnetism and crystal engineering*. [S.l.]: New York: VCH Publishers Inc, 1993.

KALARICKAL, S. S. et al. Ferromagnetic resonance linewidth in metallic thin films: Comparison of measurement methods. *Journal of Applied Physics*, American Institute of Physics, v. 99, n. 9, p. 093909, 2006.

KITTEL, C. *Physical Review*, v. 73.2, n. 155, 1948.

KITTEL, C. Introduction to solid state physics. 1976.

KOS, A. B.; SILVA, T. J.; KABOS, P. Pulsed inductive microwave magnetometer. *Review of scientific instruments*, American Institute of Physics, v. 73, n. 10, p. 3563–3569, 2002.

KRISHNAN, K. M. Magnetic materials: From isolated moments to ordered arrangements. In: *Fundamentals and Applications of Magnetic Materials*. [S.l.]: Oxford University Press, 2016.

KUROKAWA, K. *IEEE transactions on microwave theory and techniques*, v. 13, n. 2, p. 194, 1965.

LAKSHMANAN, M.; NAKAMURA, K. *Phys. Rev. Lett.*, v. 53, n. 2497, 1984.

LANDAU, L.; LIFSHITZ, E. *Phys. Z. Sowietunion*, v. 8, n. 153, 1935.

LEHMANN, U. *Manipulation of magnetic microparticles in liquid phases for on-chip biomedical analysis methods*. [S.l.], 2008.

MAKSYMOV, I. S.; KOSTYLEV, M. Broadband stripline ferromagnetic resonance spectroscopy of ferromagnetic films, multilayers and nanostructures. *Physica E: Low-dimensional Systems and Nanostructures*, Elsevier, v. 69, p. 253–293, 2015.

MALLETT, C.; GRAY, S. Autohotkey. *AutoHotkey Foundation, LLC, Charleswood, IN, USA*, 2009.

MALORATSKY, L. G.; LINES, M. Reviewing the basics of microstrip. *Microwaves RF*, v. 39, n. March, p. 79–88, 2000.

MARAMIS; J., H.; GUPTA, K. C. *Scientific Report*, v. 96, 1988.

MARQUARDT, R.; QUACK, M. *Molecular Spectroscopy and Quantum Dynamics*. [S.l.]: Elsevier, 2020.

MIYAZAKI, T.; TEZUKA, N. *J. Magn. Magn. Mater.*, v. 139, n. L231, 1995.

MONTAIGNE, F. et al. *Phys. Lett.*, v. 73, n. 2829, 1998.

MONTGOMERY, C. G.; DICKE, R. H.; PURCELL, E. M. *Principles of Microwave Circuits*. [S.l.]: McGraw-Hill, vol. 8, 1947.

MOODERA, J. S.; NOWAK, J.; VEERDONK, R. J. M. van de. *Phys. Rev. Lett.*, v. 80, n. 2941, 1998.

NEUDECKER, I. et al. Comparison of frequency, field, and time domain ferromagnetic resonance methods. *Journal of Magnetism and Magnetic Materials*, Elsevier, v. 307, n. 1, p. 148–156, 2006.

NIBARGER, J. et al. Variation of magnetization and the landé g factor with thickness in ni–fe films. *Applied physics letters*, American Institute of Physics, v. 83, n. 1, p. 93–95, 2003.

ODOM, B. et al. New measurement of the electron magnetic moment using a one-electron quantum cyclotron. *Physical review letters*, APS, v. 97, n. 3, p. 030801, 2006.

POLDER, D. Viii. on the theory of ferromagnetic resonance. *The London, Edinburgh, and Dublin Philosophical Magazine and Journal of Science*, Taylor & Francis, v. 40, n. 300, p. 99–115, 1949.

POZAR, D. M. *Microwave Engineering*. [S.l.]: J. Wiley & Sons, 4th. Ed., 2012.

SHU-HUA, L. Origine de la boussole ii. aimant et boussole. *Isis*, History of Science Society, v. 45, n. 2, p. 175–196, 1954.

SÖDERLIND, P. et al. Spin and orbital magnetism in fe-co and co-ni alloys. *Physical Review B*, APS, v. 45, n. 22, p. 12911, 1992.

SPAIN, A. V. E. *Comprehensive Materials Processing*: Sensor materials, technologies and applications. [S.l.]: Elsevier, 2014.

SPALDIN, N. A. *Magnetic materials: fundamentals and applications*. [S.l.]: Cambridge university press, 2010.

SPERLICH, A. *Electron paramagnetic resonance spectroscopy of conjugated polymers and fullerenes for organic photovoltaics*. Tese (Doutorado) — Universität Würzburg, 2013.

TAMARU, S. et al. Vector network analyzer ferromagnetic resonance spectrometer with field differential detection. *Review of Scientific Instruments*, AIP Publishing LLC, v. 89, n. 5, p. 053901, 2018.

VASILIEF, I.; GADIOU, R.; FRANKE, K. The qtiplot handbook. 2008.

WALDROP, M. M. More than moore. *Nature*, Nature Publishing Group, v. 530, n. 7589, p. 144–148, 2016.

WOLTERSDORF, G. *Spin-pumping and two-magnon scattering in magnetic multilayers*. Tese (Doutorado) — Sinon Fraser University, 2004.

XIANG, X. H. et al. *Phys. Rev. B*, v. 66, n. 174407, 2002.

YALÇIN, O. *Ferromagnetic Resonance: Theory and Applications*. [S.l.]: BoD–Books on Demand, 2013.

YIN, Y. et al. Tunable permalloy-based films for magnonic devices. *Physical Review B*, APS, v. 92, n. 2, p. 024427, 2015.

ZHANG, J. et al. Packaged microstrip line: A new quasi-tem line for microwave and millimeter-wave applications. *IEEE Transactions on Microwave Theory and Techniques*, IEEE, v. 65, n. 3, p. 707–719, 2016.

ZHANG, S.; LEVY, P. M.; FERT, A. *Phys. Rev. Lett.*, v. 88, n. 236601, 202.

ZHANG, S. et al. *Phys. Rev. Lett.*, v. 79, n. 3744, 1997.

ZHAO, Y. et al. Experimental investigation of temperature-dependent gilbert damping in permalloy thin films. *Scientific reports*, Nature Publishing Group, v. 6, n. 1, p. 1–8, 2016.

Appendix

A

VNA-FMR Software

This is the last version of the computer based software. It is based on the Autohotkey macro-language and also depends on a serial port manager configure appropriately. It establishes connections with the several equipment, controls experimental points flux acquisition, controls the VNA, the arduino and the PSU (this one only for the step-field sweep technique) and saves data at the request of the experimenter.

```
#NoEnv  ; Recommended for performance and compatibility with future AutoHotkey releases.
#Warn  ; Enable warnings to assist with detecting common errors.
SendMode Input  ; Recommended for new scripts due to its superior speed and reliability.
SetWorkingDir %A_ScriptDir%  ; Ensures a consistent starting directory.
SetTitleMatchMode,  1 ; window prefix name match

SetFormat, float, 0.2E
FreqCentral = 10.0E09 ;Campo Inicial em mT
Span = 0.0
Marker = 10.0E09


SetFormat, float, 0.4E
tempo = 31.0014E-3 ;Tempo de aquisição (1/2 onda)

tempo2 := 0.0
Medias = 50.0
MediasCal = 50.0

Flagtrg = 1
```

```
Flaghold = 1
Flagkep = 1
Smooth = 10

Run, putty.exe ;Inicialização Arduino
Sleep, 50 ; cada unidade adiciona ~1.3ms
WinActivate, PuTTy
Sleep, 50
Send {Tab} {Tab} {Tab} {Tab}  ;send 4 tabs
Send {Down}
Send {Enter}
Sleep, 1000

; VNA communication initialization
Run, putty.exe ;Inicialização VNA
Sleep, 50 ; cada unidade adiciona ~1.3 ms
WinWait PuTTY
WinActivate  ; Uses the last found window.
Sleep, 50
Send {Tab} {Tab} {Tab} {Tab}  ;send 4 tabs
Send {Down} {Down} {Down}
Send {Enter}
Sleep, 1000

;Inicialização KEPCO
;Run, putty.exe
;Sleep, 50 ; cada unidade adiciona ~1.3ms
;WinActivate, PuTTy
;Sleep, 50
;Send {Tab} {Tab} {Tab} {Tab}  ;send 4 tabs
;Send {Down}{Down}{Down}{Down}
;Send {Enter}
;Sleep, 1000

Gui 1:Add, Button, w115 y10 gLoadLIA, Load VNA LIA setup
Gui 1:Add, Button, w115 gCalVNA, &Calibrate VNA
;Gui 1:Add, Button, w115 gKEPCO , On/off &KEPCO
Gui 1:Add, Button, w115 gTrigger, Int/Ext &trigger
Gui 1:Add, Button, w115 gArduinoS, &Start/stop H Field
```

```
Gui 1:Add, Button, w115 y10 x+5 gInc100mhz, +100 MHz
Gui 1:Add, Button, w115 y+6 gInc1ghz, &+1 GHz
Gui 1:Add, Button, w115 y+6 gDec1ghz, &-1 GHz
;Gui 1:Add, Button, w115 y+6 gTrigger, Int/Ext trigger
Gui 1:Add, Button, w115 y+6 gDec100mhz, -100 MHz

Gui 1:Add, Button, w90 y10 gClearAVG, C&lear averages
;Gui 1:Add, Button, w90 y10 gSaveSNP, Save SNP2
Gui 1:Add, Button, w90 y+6 gSmooth, S&mooth
;Gui 1:Add, Button, w90 y+6 gSaveTraces, Save Traces
Gui 1:Add, Button, w90 y+6 gHoldTrigger, &Hold trigger
Gui 1:Add, Button, w90 y+6 gAutoscale, &Autoscale

Gui 1:Add, Text, x10 y+6, Salvar em  :
Gui 1:Add, Edit, vDirSpec w335, d:\perm100nm_lia_angulo

Gui 1:Add, Text, ,Nome base do arquivo + _##GHz :
Gui 1:Add, Edit, vNomeArquivo w335, PtCo08A
Gui 1:Add, Button, x111 y+6 w75 gSaveField, Save Field
Gui 1:Add, Button, x+5 w75 gSaveSNP, Save SNP2
Gui 1:Add, Button, x+5 w75 gSaveTraces, Save Traces
Gui 1:Add, Button, x+5 w75 gQuitter, Exit

Gui 1:Show
if WinExist("FMR_GUI") ; janela do organizador
   {
WinActivate  ; Uses the last found window.

   }
Return

LoadLIA:
if WinExist("VNA") ; janela do VNA
   {
WinActivate  ; Uses the last found window.
Sleep, 100
       Send :MMEMORY:LOAD:STATE "D:\fmr_lia.sta" {Enter}
Sleep 1000
```

```
SetFormat, float, 0.1E
Send :SENS1:FREQ:CENT %FreqCentral% {Enter}
Sleep, 1000
Send :SENS1:FREQ:SPAN %Span% {Enter}
Sleep, 1000
   }
   if WinExist("FMR_GUI") ; janela do organizador
      {
WinActivate  ; Uses the last found window.

      }
Return

CalVNA:
   if WinExist("VNA") ; janela do VNA
   {
WinActivate  ; Uses the last found window.
        Sleep, 1000
Send :SENS:AVER:COUN %MediasCal% {Enter} ;max averages
Sleep 1000
Send :TRIGGER:SOURCE INT {Enter}
Sleep, 1000
Send :SENS1:CORR:COLL:METH:THRU 2,1 {Enter} ;specify cal method
Sleep, 1000
Send :SENS1:CORR:COLL:THRU 2,1 {Enter} ;measure cal data
SetFormat float, 0.4E
tempo2 := Round(MediasCal * tempo * 1200)
Sleep, tempo2
Send :SENS1:CORR:COLL:SAVE {Enter}
Sleep, 1000
Send :SENS:AVER:COUN %Medias% {Enter} ;mrm averages
Sleep 1000
Send :TRIGGER:SOURCE EXT {Enter}
Sleep, 1000
   }
   if WinExist("FMR_GUI") ; janela do organizador
      {
WinActivate  ; Uses the last found window.
```

```
      }
Return

KEPCO:
   if Flagkep = 1
{
   if WinExist("COM1") ; janela da KEPCO
    {
WinActivate  ; Uses the last found window.
        Sleep, 1000
Send :SYST:REM OFF {Enter}
Sleep, 1000
}
Flagkep = 0
}
   else
{
   if WinExist("COM1")
    {
WinActivate  ; Uses the last found window.
         Sleep, 1000
Send :SYST:REM ON {Enter}
;Send :OUTP ON {Enter}
;Send :CURR 0 {Enter}
Sleep, 1000
}
Flagkep = 1
}
   if WinExist("FMR_GUI") ; janela do organizador
      {
WinActivate  ; Uses the last found window.

      }
Return

ArduinoS:
if WinExist("Arduino")
{
WinActivate
```

```
Sleep, 100
Send s {Enter} ;restart field
Sleep, 1000
}
   if WinExist("FMR_GUI") ; janela do organizador
      {
WinActivate  ; Uses the last found window.

      }
Return

ClearAVG:
   if WinExist("VNA") ; janela do VNA
   {
WinActivate  ; Uses the last found window.
        Sleep, 1000
Send :SENS:AVER:CLE {Enter}
Sleep, 1000
   }
   if WinExist("FMR_GUI") ; janela do organizador
      {
WinActivate  ; Uses the last found window.

      }
Return

Inc1ghz:
SetFormat float, 0.2E
FreqCentral += 1.0E09
if (FreqCentral > 18.0E9)
   FreqCentral = 18.0E9
if WinExist("VNA") ; janela do VNA
   {
FreqCentral := StrReplace(FreqCentral, "+") ;bug da linguagem...
WinActivate  ; Uses the last found window.
        Send :SENS1:FREQ:CENT %FreqCentral% {Enter}
Sleep, 1000
   }
   if WinExist("FMR_GUI") ; janela do organizador
```

```
      {
WinActivate  ; Uses the last found window.

      }
Return

Inc100mhz:
SetFormat float, 0.2E
FreqCentral += 0.1E09
;msgbox, %FreqCentral%
if (FreqCentral > 18.0E9)
   FreqCentral = 18.0E9
if WinExist("VNA") ; janela do VNA
   {
FreqCentral := StrReplace(FreqCentral, "+") ;bug da linguagem...
WinActivate  ; Uses the last found window.
        Send :SENS1:FREQ:CENT %FreqCentral% {Enter}
Sleep, 1000
   }
   if WinExist("FMR_GUI") ; janela do organizador
      {
WinActivate  ; Uses the last found window.

      }
Return

Dec1ghz:
SetFormat float, 0.2E
FreqCentral -= 1.0E09
if (FreqCentral < 1.0E09)
   FreqCentral = 1.0E9
if WinExist("VNA") ; janela do VNA
   {
FreqCentral := StrReplace(FreqCentral, "+") ;bug da linguagem...
WinActivate  ; Uses the last found window.
        Send :SENS1:FREQ:CENT %FreqCentral% {Enter}
Sleep, 1000
   }
   if WinExist("FMR_GUI") ; janela do organizador
```

```
      {
WinActivate  ; Uses the last found window.

      }
Return

Dec100mhz:
SetFormat float, 0.2E
FreqCentral -= 0.1E09
if (FreqCentral < 0.1E9)
   FreqCentral = 0.1E9
if WinExist("VNA") ; janela do VNA
   {
FreqCentral := StrReplace(FreqCentral, "+") ;bug da linguagem?
WinActivate  ; Uses the last found window.
        Send :SENS1:FREQ:CENT %FreqCentral% {Enter}
Sleep, 1000
   }
   if WinExist("FMR_GUI") ; janela do organizador
      {
WinActivate  ; Uses the last found window.

      }
Return

Trigger:
   if Flagtrg = 1
{
   if WinExist("VNA") ; janela do VNA
    {
WinActivate  ; Uses the last found window.
        Sleep, 1000
Send :TRIGGER:SOURCE INT {Enter}
Sleep, 1000
}
Flagtrg = 0
}
   else
{
```

```
   if WinExist("VNA") ; janela do VNA
    {
WinActivate  ; Uses the last found window.
        Sleep, 1000
Send :TRIGGER:SOURCE EXT {Enter}
Sleep, 1000
}
Flagtrg = 1
}
   if WinExist("FMR_GUI") ; janela do organizador
      {
WinActivate  ; Uses the last found window.

      }
Return

Smooth:
   if Smooth = 1.5
{
   if WinExist("VNA") ; janela do VNA
    {
WinActivate  ; Uses the last found window.
        Sleep, 1000
Send :CALC1:PAR1:SEL{Enter}
Send :CALC1:SMO:APER 3.5 {Enter}
Send :CALC1:PAR2:SEL{Enter}
Send :CALC1:SMO:APER 3.5 {Enter}
Sleep, 1000
}
Smooth = 3.5
}
   else if Smooth = 3.5
{
   if WinExist("VNA") ; janela do VNA
    {
WinActivate  ; Uses the last found window.
        Sleep, 1000
Send :CALC1:PAR1:SEL{Enter}
Send :CALC1:SMO:APER 10 {Enter}
```

```
Send :CALC1:PAR2:SEL{Enter}
Send :CALC1:SMO:APER 10 {Enter}
Sleep, 1000
}
Smooth = 10
}
   else if Smooth = 10
{
   if WinExist("VNA") ; janela do VNA
    {
WinActivate  ; Uses the last found window.
         Sleep, 1000
Send :CALC1:PAR1:SEL{Enter}
Send :CALC1:SMO:APER 1.5 {Enter}
Send :CALC1:PAR2:SEL{Enter}
Send :CALC1:SMO:APER 1.5 {Enter}
Sleep, 1000
}
Smooth = 1.5
}
   if WinExist("FMR_GUI") ; janela do organizador
      {
WinActivate  ; Uses the last found window.

      }
Return

SaveField:
 Gui, Submit, NoHide
if WinExist("Arduino")
   {
   WinActivate
   ; No putty "Lines of scrollback especificado como nr_pontos - 50.
   WinMenuSelectItem, Arduino,, 0&, Copy All to Clipboard
   Sleep, 100
   FreqCen1 := StrReplace(FreqCentral, ".", "_")
   FreqCen1 := StrReplace(FreqCen1, "E09","G")
   FreqCen1 := StrReplace(FreqCen1, "E06","M")
   Fileappend,%Clipboard%, %DirSpec%\%NomeArquivo%_Campo_%FreqCen1%Hz.csv
```

```
   }
   if WinExist("FMR_GUI") ; janela do organizador
      {
WinActivate  ; Uses the last found window.

      }
Return

SaveSNP:
   Gui , Submit, NoHide
   if WinExist("VNA") ; janela do VNA
   {
WinActivate  ; Uses the last found window.
        Sleep, 1000
FreqCen1 := StrReplace(FreqCentral, ".", "_")
FreqCen1 := StrReplace(FreqCen1, "E09","G")
FreqCen1 := StrReplace(FreqCen1, "E06","M")

Send :MMEM:STOR:SNP:TYPE:S2P 2,1 {Enter}
Sleep, 100
Send :MMEM:STOR:SNP "%DirSpec%\%NomeArquivo%_%FreqCen1%Hz.S2P" {Enter}
Sleep, 3000
   }
   if WinExist("FMR_GUI") ; janela do organizador
      {
WinActivate  ; Uses the last found window.

      }
Return

SaveTraces:
   Gui, Submit, NoHide
   if WinExist("VNA") ; janela do VNA
   {
FreqCen1 := StrReplace(FreqCentral, ".", "_")
FreqCen1 := StrReplace(FreqCen1, "E09","G")
FreqCen1 := StrReplace(FreqCen1, "E06","M")

WinActivate  ; Uses the last found window.
```

```
        Sleep, 1000
Send :CALC1:PAR1:SEL{Enter}
Sleep, 100

Send :MMEM:STOR:FDAT "%DirSpec%\%NomeArquivo%_%FreqCen1%Hzr.csv"{Enter}
Sleep, 3000

Send :CALC1:PAR2:SEL{Enter}
Sleep, 100
Send :MMEM:STOR:FDAT "%DirSpec%\%NomeArquivo%_%FreqCen1%Hzi.csv"{Enter}
Sleep, 3000
   }
   if WinExist("FMR_GUI") ; janela do organizador
      {
WinActivate  ; Uses the last found window.

      }
Return

HoldTrigger:
   if Flaghold = 1
{
   if WinExist("VNA") ; janela do VNA
    {
WinActivate  ; Uses the last found window.
         Sleep, 1000
Send :INIT1:CONT OFF {Enter}
Sleep, 1000
}
Flaghold = 0
}
   else
{
   if WinExist("VNA") ; janela do VNA
    {
WinActivate  ; Uses the last found window.
         Sleep, 1000
Send :INIT1:CONT ON {Enter}
Sleep, 1000
```

```
}
Flaghold = 1
}
   if WinExist("FMR_GUI") ; janela do organizador
      {
WinActivate  ; Uses the last found window.

      }
Return
Autoscale:
   if WinExist("VNA") ; janela do VNA
   {
WinActivate  ; Uses the last found window.
        Sleep, 1000
Send :DISPLAY:WIND1:TRAC1:Y:AUTO {Enter} ;autoscale trace
Sleep 1000
Send :DISPLAY:WIND1:TRAC2:Y:AUTO {Enter}
Sleep 1000
   }
if WinExist("FMR_GUI") ; janela do organizador
   {
WinActivate  ; Uses the last found window.

   }
Return

GuiEscape:
GuiClose:
Quitter:
   Winclose, VNA
   Winclose, Arduino
   Winclose, COM1
ExitApp
```

B

Arduino Software

This is the synchronized-field sweep version of the arduino program. A highly specialized piece of software with many parts written in a way to directly access some of the arduino's registers in order to achieve maximum performance in for the generation of the square signal. Warning: Very difficult to read for the non-initiated.

```
   /*
 * Board:Arduino pro-mini
 * Atmega168
 * Programmer: AVRISP
 * PWM outputs: D9 and D10 (~8 kHz)
 * ADC input: A0 (oversampled)
 *
 * dXXXX: delay in ms between PWM output and ADC reading
 * gXXXX: send immediatelly XXXX to PWM and get a single ADC measurement
 * s: start/stop running loop measurement
 * bXXXX: bottom PWM value for loop measurement (from 0 to 1000)
 * tXXXX: top PWM value for loop measurement  (from 24 to 1023)
 * r: reset PWM value
 * z: zero field reading (off-set correction)
 *
 */


//timer1 (16 bits) does PWM for pins 9 and 10


int PWMin = 0, PWMax = 1024, PWM = 256;
float B = 0, OS = 0;
```

```
unsigned int AD[200];
int n = 200;
int dly = 500;
bool trigger = 1;
bool prn_field = 1;
byte avg = 20; //number of averages fol field measurement
int counter=0;
void setup() {
  config_adc();
  config_timer1();
  Serial.begin(115200);  // initialize serial:
    pinMode(A0, INPUT);
    pinMode(9, OUTPUT);
    pinMode(10, OUTPUT);
     OCR1AH = PWM >> 8;
     OCR1AL = PWM & 0xFF;
     OCR1BH = PWM >> 8;
     OCR1BL = PWM & 0xFF;
     //Serial.print(PWM);
     //Serial.print(", ");
     delay(dly-5);

}


void loop() {
     //delayMicroseconds(1022);//adjust to start at the minimum field
     while (trigger == 0){
      TCCR1B = 1; //freq PWM = 7800 Hz
      if (Serial.available() > 0) {  serialRead(); }
      prn_field = 1;  //enable sending field values
      }
      TCCR1B = 5; //freq PWM = 7.8 Hz
       (Kepco current follows this low frequency)
     if (Serial.available() > 0) {
      serialRead(); // if there's any serial character available, read it
     }
//      counterL = TCNT1L; //need to read first LOW byte TCNT1L
//      counterH = TCNT1H;      // to access HIGH byte TCNT1H
```

```
   if (prn_field == 1){
    delay(500);//wait for the field to stabilize
   for (int m = 0; m < avg; m++){
     counter = TCNT1L + (TCNT1H << 8);
     while (counter < 510){counter = TCNT1L + (TCNT1H << 8);}
      while (counter > 231){counter = TCNT1L + (TCNT1H << 8);}
      for (int i = 0; i < n; i++){
       AD[i] += ADCRead(); //accumulate measurements for averaging
//        AD[i] = (AD[i] + ADCRead()) >> 1;    //AD[i] * 0.98 + 0.02 * ADCRead();
        // EWMA not implemented due to low memory (AD[i] must be float)
        delayMicroseconds(134); to get a complete VNA acquisition
        //VNA Trigger edge: positive (TCNT1H>0)
         }
       } //end of for
      for (int i = 0; i < n; i++){
        Serial.println(float(AD[i])/avg*0.4227+0.82);
        //send field calibrated in mT at sample position with hall probe at pole
        AD[i] = 0;   }
          // Serial.println(""); //send blank line
           prn_field = 0; //disable sending field values
      } //end of if


  //    if (trigger == 0){PWM = PWMax;}


}


 void serialRead(){
   char  received = Serial.read();
//           Serial.print(received);

  switch (received) {
      case 'n':
      case 'N':
          n = Serial.parseInt();
          n = constrain(0, 0, 65536);
```

(stop at maximum field)

```
        if (Serial.read() == '\n' || Serial.read() == '\r') {}
      break;

    case 'b':
    case 'B':
        PWMin = Serial.parseInt();
        PWMin = constrain(PWMin, 0, PWMax-1);
        if (Serial.read() == '\n' || Serial.read() == '\r') {}
      break;


    case 't':
    case 'T':
        PWMax = Serial.parseInt();
        PWMax = constrain(PWMax, PWMin+1, 1023);
        if (Serial.read() == '\n' || Serial.read() == '\r') {}
      break;

//      case 'g':
//      case 'G':
//          PWM = Serial.parseInt();
//          PWM = constrain(PWM, 0, 1023);
//          if (Serial.read() == '\n' || Serial.read() == '\r') {}
//          get_meas();
//       break;

    case 'd':
    case 'D':
        dly  = Serial.parseInt();
        dly   = constrain(dly, 10, 5000);
        if (Serial.read() == '\n' || Serial.read() == '\r') {}

    break;

    case 'r':
    case 'R':
          PWM = PWMin;
    break;
```

```
      case 's':
      case 'S':
            trigger = !trigger;
      break;


      case 'z':
      case 'Z':
            OS = B;
      break;

      default :
      if (Serial.read() == '\n' || Serial.read() == '\r') {};
      }
}

 int ADCRead(){

  ADCSRA |= (1 << ADSC);            //  Start the conversion
  while (ADCSRA & (1 << ADSC));
  int sample  = ADCL;//8 LSBs of the result
  sample += ADCH<<8; //2 MSBs of the result
  return sample;

  }

/*
void get_meas(){

     OCR1AH = PWM >> 8;
     OCR1AL = PWM & 0xFF;
     OCR1BH = PWM >> 8;
     OCR1BL = PWM & 0xFF;
     Serial.print(PWM);
     Serial.print(", ");
     delay(dly-5);

    for (int i = 0; i < n; i++){
       AD += ADCRead();
```

```
    }
      B = (AD/n-512)/2.048;
      Serial.println(B - OS, 1);
      AD = 0;

}
*/
void config_adc(){

   ADCSRA &= ~0b111;        // ADC prescaler = 32 (default = 128)
   ADCSRA |= 0b101;
   ADMUX = 0b01000000;      //select ref voltage 5 V and channel A0
}


void config_timer1() {
  //Waveform Generation Mode 3 : PWM, Phase Correct, 10-bit
  TCCR1A = 0b10100010;    // correct phase PWM, 10 bits (WGM10=11)
  TCCR1B = 0b00000101;  //clk sys = 16MHz + WGM32:
  TIFR1 = 0;   //CTC operating mode (WGM32=00) fout= 7.8 Hz
  ICR1H = 0xFF; // set TOP to 16bit
  ICR1L = 0xFF; // set TOP to 16bit
  OCR1AH = 0x00;
  OCR1AL = 0x00;
  OCR1BH = 0x00;
  OCR1BL = 0x00;

  }
```